ALMA MATER STUDIORUM
UNIVERSITA' DI BOLOGNA

SCUOLA DI INGEGNERIA E ARCHITETTURA
-Sede di Forlì-

CORSO DI LAUREA
IN INGEGNERIA AEROSPAZIALE
Classe: L-9

ELABORATO FINALE DI LAUREA IN

AERODINAMICA DEGLI AEROMOBILI

SEPARATION CONTROL BY MEANS OF ORIENTED DBD PLASMA ACTUATORS: AN EXPERIMENTAL ANALYSIS IN A WIND TUNNEL

CANDIDATO
Lucia Mascotelli

RELATORE
Chiar.mo. Prof.
Alessandro Talamelli

CORRELATORE
Dr. Alessandro Rossetti
Prof. A. Cristofolini
Prof. G. Neretti

Anno Accademico 2012/2013
Sessione: I

La terra ci fornisce, sul nostro conto, più insegnamenti di tutti i libri.
Perché ci oppone resistenza.
Misurandosi con l'ostacolo l'uomo scopre se stesso.
Ma per riuscirci gli occorre uno strumento.
Gli occorre una pialla, o un aratro.
Il contadino, nell'arare, strappa a poco a poco alcuni segreti alla natura,
e la verità ch'egli trae è universale.
Non diversamente l'aeroplano, strumento delle vie aeree,
coinvolge l'uomo in tutti gli antichi problemi.

[Antoine de Saint-Exupéry, *Terra degli uomini*]

Abstract

This thesis provides an experimental analysis of the effectiveness of oriented DBD plasma actuators over a NACA 0015 airfoil at low Reynolds numbers. Tests were performed in partnership with the Department of Electrical Engineering of Bologna University, in the wind tunnel of the Applied Aerodynamics Laboratory of Aerospace Engineering faculty.

Lift coefficient measurements were carried out in order to verify how an oriented plasma jet succeeds in prevent boundary layer separation. Both actuators' chord wise position and plasma jet orientation angle have been investigated to examine which configurations lead to the best results. A particular attention has been paid also to the analysis of results in steady and unsteady plasma actuation.

Questa tesi offre un'analisi sperimentale sull'efficacia di attuatori al plasma orientabili, basati su una tecnologia DBD, installati su un profilo alare NACA 0015, a bassi numeri di Reynolds. Le prove sono state condotte in collaborazione con il Dipartimento di Ingegneria Elettrica dell'Università di Bologna, nella galleria del vento del Laboratorio di Aerodinamica Applicata della Facoltà di Ingegneria Aerospaziale di Forlì.

Per verificare come un getto orientabile di plasma riesca a prevenire la separazione dello strato limite, sono state eseguite misure sul coefficiente di portanza. Sono state indagate sia la posizione degli attuatori lungo la corda che l'angolo con cui è orientato il getto di plasma, per vedere quali configurazioni conducono ai migliori risultati. Una particolare attenzione è stata riservata all'analisi dei risultati ottenuti con plasma continuo e pulsato.

INDEX

LIST OF FIGURES

LIST OF TABLES

INTRODUCTION

During a flight, the aircraft's wings have to face very different situations, and therefore, different characteristics and behaviour are required. In a cruise regime, for instance, wings must have some features that allow friction drag reduction, but, on the other hand, wings play an important role also in landing and taking off, when the velocities are much smaller and the main result desired is the increase in lift coefficient.

Reaching a higher lift coefficient is possible by increasing the angle of attack, the angle of the wing respect the flow. Nevertheless, this operation has to be done carefully, since, if the angle of attack is higher than the maximum angle, known as the stall angle, the boundary layer will be subjected to the phenomenon called "boundary layer separation", and the aircraft's performances will decay.

To overcome this problem, the solution is controlling the flow passing past the wing.

The flow control devices' family groups two main types of apparatus: active and passive devices, depending on their need of external powering.

While the active methods need an external source of power to work, the passive methods don't. An example of the first type of control method is a suction of low energy particles adjacent to the surface through a pump system, or re-energising them by blowing thin jets. Passive methods, on the other hand, features devices such vortex generators, that, creating vortexes favour the mixing of particles, bringing the higher kinetic energy particles near the surface, replace the lower energy ones.

Despite being cheaper, easier to realise and not requiring any added power, passive flow control devices have important practical disadvantages. In fact, they are present even when not required, during cruise for instance, leading to higher drag. That's why for few years the topic of active flow control has been growing constantly. Among all the active methods a new and original technology using DBD plasma actuators is in full expansion from early 1990s. Although mechanical devices are effective, they have some drawbacks. Complicated in realisation, add in weight, non negligible volume, source of

noise and always present possibility of failure are the downsides of mechanical active methods. Thus, since the plasma actuators don't exhibit all these problems and are easy to install, not to mention the fact they're not cumbersome, curiosity and studies around them, especially for aerodynamics use, are ever growing.

In particular, since already numerous research groups all over the world tested the effectiveness of plasma actuators installed over an airfoil at low Reynolds numbers, Department of Industrial Engineering in partnership with Department of Electrical Engineering have decided to test the effectiveness of a vectoring in plasma jet direction.

In particular, plasma actuators had been installed over a NACA 0015 airfoil and tests inside the wind tunnel of the Applied Aerodynamics Laboratory had been carried out.

The aim is, then, to demonstrate how an oriented jet of plasma can help separation control and therefore delay the stall condition, through lift, and consequently lift coefficient, measurements.

An aerodynamics background as well as a literature review on plasma actuators is presented in chapter 1, while in chapter 2 is described the experimental set up needed to carry out the tests and the method used. The results obtained are shown in chapter 3, with some considerations on plasma actuators' effect on flow. Conclusions on the effectiveness of oriented DBD plasma actuators are reported in chapter 4.

CHAPTER 1

THEORY

In this chapter we are going to talk about aerodynamics theory, paying particular attention to boundary layer separation and its connection to lift. We are then going to describe flow control devices, focusing on plasma actuators in particular.

1.1 Boundary Layer

A fundamental result of analysis of a flow past a slender body (an airfoil for example), is that, if the typical Reynolds number of the flow is large and the viscosity μ is relatively small, then vorticity may remain confined in regions of small thickness adjacent to the body from whose surface it has been generated and in a thin wake trailing downstream. This flow region is known as boundary layer, and it's the region where the effect of viscosity is felt, while in the outer irrotational flow, the particles moves as if they belonged to a non-viscous fluid.

Within these boundary layers, however, large shearing velocities are produced with consequent shearing stresses of appreciable magnitude. The presence of intermolecular forces between solids and fluids leads to the assumption that at the boundary between a solid and a fluid there is a condition of no slip. This means that the relative velocity of the fluid tangential to the surface is everywhere zero.

Where the boundary layer is present, velocity gradients become appreciable: the velocity varies rapidly from zero at the surface of the body to the value of the free stream velocity, characteristic of the outer flow. The boundary layer velocity profile over a flat plate parallel to the flow has the trend described in picture 1.1

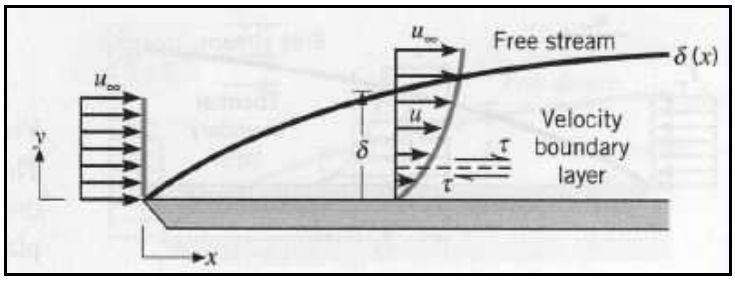

Figure 1.1: Boundary Layer velocity profile over a flat plate

Where $\delta(x)$ is the boundary layer thickness, conventionally defined as the distance within which 99% of the total vorticity present along a line normal to the surface is contained.

Prandlt first suggested that, provided a body satisfies certain restrictions regarding both its shape (body of a slender form) and its motion (at moderate angle of attack to the flow and a sufficiently high Reynolds number), the thickness of the Boundary Layer is usually very small. As a first approximation, then, the presence of the Boundary Layer can be neglected, in order to estimate the pressure field produced about the body. When boundary layer around a body remains thin and attached, the flow field and the related loads can be analysed and predicted using a much simplified iterative procedure, which implies consecutive solutions of the outer irrotational flow and of the boundary layer equation. More importantly Prandlt showed that the pressure is practically constant across the boundary layer. This result permits linking the pressure on the body surface to that acting on the flow outside the boundary layer, where the equations to be satisfied coincide with those of a non-viscous fluid.

Since almost the full lifting force is produced by normal pressures at the airfoil surface, it's possible to develop theories for the evaluation of the lift force by consideration of the flow field outside the boundary layers. This is essential to a complete aerodynamic study of a body, because, unlike the potential theory, it considers the shearing stresses at the body surface, allowing the estimation of the drag force.

1.1.1 Boundary Layer Prandtl's equations

Let us consider a two-dimensional flow past a flat surface and parallel to it. We assume the existence of a boundary layer, characterized by a thickness small compared to any linear dimension L in which velocity variation occur in the x direction. In other words,

$\delta/L<<1$. Considering that through the boundary layer the velocity varies more rapidly than in x direction, we may use the following approximations:

$$\left|\frac{\partial^2 u}{\partial x^2}\right| << \left|\frac{\partial^2 u}{\partial y^2}\right| \quad , \quad \left|\frac{\partial^2 v}{\partial x^2}\right| << \left|\frac{\partial^2 v}{\partial y^2}\right| \tag{1.1}$$

Consequently, considering a two-dimensional flow parallel to the surface and neglecting the effect of body forces, the momentum balance equations in x and y direction become:

$$\frac{\partial u}{\partial t} + u\frac{\partial u}{\partial x} + v\frac{\partial u}{\partial y} = -\frac{1}{\rho}\frac{\partial p}{\partial x} + \upsilon\frac{\partial^2 u}{\partial y^2} \tag{1.2}$$

$$\frac{\partial v}{\partial t} + u\frac{\partial v}{\partial x} + v\frac{\partial v}{\partial y} = -\frac{1}{\rho}\frac{\partial p}{\partial y} + \upsilon\frac{\partial^2 v}{\partial y^2} \tag{1.3}$$

The mass conservation equation is:

$$\frac{\partial u}{\partial x} + \frac{\partial v}{\partial y} = 0 \tag{1.4}$$

that leads to the assumption that the velocity component normal to the surface, v, is smaller that the tangential component u: $v<<u$, in the same way that $\delta<<L$.

We can now carry out an order of magnitude analysis of the equations. Using all the assumptions made, we can see that the momentum equation in the y direction, normal to the wall, is reduced with a very good approximation, to:

$$\frac{\partial p}{\partial y} = 0 \tag{1.5}$$

Therefore, the relation above, states that the pressure variations across the boundary layer thickness is negligible. This means that the pressure within the boundary layer is equal to the pressure in the outer region, considering the same x position:

$$p(x,0) = p(x, \delta) \tag{1.6}$$

This is a crucial result of Prandtl's boundary layer theory, since it allows us to couple the pressure distribution within the boundary layer to the one of the outer potential flow. Moreover we can evaluate pressure distribution as a function of the velocity in the outer region $U_e(x)$. Adding the boundary conditions:

$$\text{at the surface (y = 0) : } u = v = 0 \text{ ;} \qquad (1.7)$$
$$\text{at the edge (y = ye) : } u = U\text{e ;}$$

The pressure variation is then given by the relation:

$$-\frac{1}{\rho}\frac{\partial p(x)}{\partial x} = \mathrm{Ue(x)}\frac{\partial \mathrm{Ue(x)}}{\partial x} \qquad (1.8)$$

1.1.2 Boundary Layer Separation

Let us consider a flat plate, parallel to a two-dimensions flow. For Reynolds number sufficiently high, the velocity outside the boundary layer is nearly uniform, hence, for Bernoulli's theorem:

$$\frac{p}{\rho} + \frac{\left|V^2\right|}{2} = const \qquad (1.9)$$

even the pressure is constant. Therefore, knowing that pressure is constant across the boundary layer, the boundary layer is not subjected to any pressure gradient. We can then say that the term $\frac{\partial p(x)}{\partial x}$ is zero.

If we now consider a body of any shape, for example an airfoil, the velocity in the outer region is not uniform anymore. In particular, the motion field is characterized by a front stagnation point A on the body surface[fig 1.2]

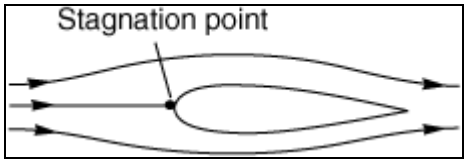

Figure 1.2: Front stagnation point

In this point, the pressure will reach its maximum value, that, for Bernoulli's theorem, will be:

$$p_A = p_\infty + \frac{1}{2}\rho U^2 \qquad (1.10)$$

where p_∞ is the value of the pressure of the flow upstream, undisturbed.

From A up until the point of maximum thickness the flow accelerates, therefore, the pressure tends to decrease. Thanks to the increasing velocity, the boundary layer thickness tends to become smaller, behaving as if the particles were "pushed" to the surface of the body. For this reason the negative pressure gradient is generally referred to as *favourable* pressure gradient. In the same way, when a boundary layer is subjected to a positive pressure gradient in the flow direction, the flow tends to decelerate. This implies an increasing boundary layer thickness. If the positive pressure gradient is strong enough, and it acts over a sufficiently long surface extension, the boundary layer does not remain attached to the surface, and the boundary layer separation phenomenon can be generated.

Let us consider, then, a portion of surface where the flow is subjected to a positive pressure gradient, known as *adverse* pressure gradient. Following the body surface, we see the evolution of the boundary layer velocity profile [fig 1.3]:

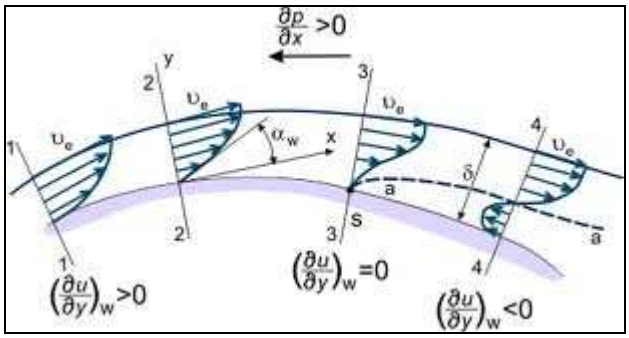

Figure 1.3: Boundary layer velocity profile evolution

The change in shape of the velocity profile consists in a progressive upward displacement of the inflection point and in a rapid reduction of the velocity close to the surface. This is due to the fact that every particle within the boundary layer is subjected to the same pressure force directed against the motion, but their kinetic energy is not the same.

In particular, the adverse pressure gradient will slow down more the particles moving near the wall, and less the ones nearer to the edge of the boundary layer, since their velocity is greater. So we can find a specific point, S, on the surface, where the separation takes place: the separation point. It corresponds to a particular velocity condition:

$$\left.\frac{\partial u}{\partial y}\right|_w = 0$$

Beyond that point, the particles near the wall move backwards, generating a retrograde flow. The irrotational flow is then strongly pushed away from the surface, outwards. The region where vorticity is confined, is then no longer thin or close to the surface, but it will fill the entire downstream separated region , forming a wake. This leads to a drastic change to the outer potential flow in respect to the condition of attached boundary layer. Consequently, after the separation point, boundary layer theory is not valid, because pressure distributions got with a potential theory (neglecting the presence of vorticity into field), is no more an approximation of their real trend.

Experience shows that a positive pressure gradient is a strictly necessary condition only for separation along slightly curved surfaces, while it always occurs in presence of asperities. This happens because sharp edges are characterized by strong adverse pressure gradients, unsustainable without separation.

We shall now briefly analyse the case of turbulent boundary layer. Its peculiar features are vortical structures, inclined in the flow direction, and strong mixing mechanisms. Because of the mixing, the turbulent flow brings higher velocity particles of the outer region towards the region closer to the wall. This justifies the stronger viscous stresses over the surface and the higher velocity near the surface. Consequently, turbulent boundary layers are much more resistant to adverse pressure gradients, producing a delay of separation.

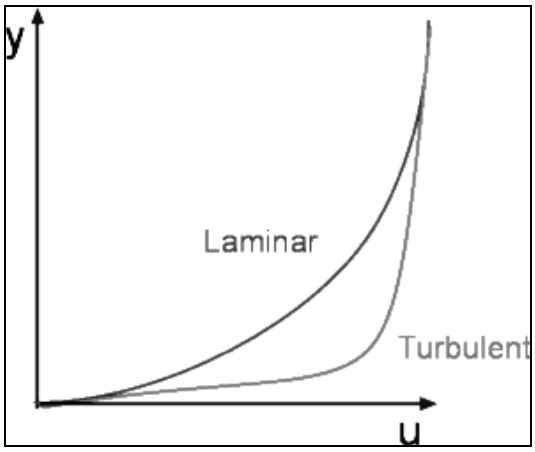

Figure 1.4: Comparison between turbulent and laminar velocity profile

Under certain condition of Reynolds number the generation of the laminar separation bubble is possible. After having experienced separation, the flow becomes turbulent and can re-attach to the surface.

1.1.3 Laminar Separation

The separation bubble, or laminar separation, is a phenomenon typical of low Reynolds number flows. When the pressure gradient is adverse enough and acts over a sufficiently large portion of surface, the boundary layer can experience separation. Further downstream, the adverse pressure is driving the inner layers backward, although the outer layers are still moving forward. When they meet, since they can't go through the surface, the only possible solution is to turn away from the surface. Right after the separation, the pressure distribution becomes constant and the flow unstable.

In particular, under certain conditions of Reynolds number and angle of attack, the separation can occur at the leading edge. The sensibility of the flow to transition becomes very high, leading to a very fast transition from laminar to turbulent. This phenomenon implies an increasing entrainment, that can induce the flow, now turbulent, to re-attach to the surface. The separation bubble is then generated.

In two-dimensional flow, the result is a streamline connecting the separation and reattachment points, with the fluid between the dividing streamline and the wall recirculating endlessly. In three dimensional situations, if the separation or re-attachment lines are swept, the streamlines from the separation points can spiral up the bubble inside the

streamlines to the reattachment points, forming a vortex sheet. This means that fluid can escape out the ends of the bubble, and can be seen by observing the tell tails. In fact, they will point up instead of backwards or forward (respectively outside and inside the bubble).

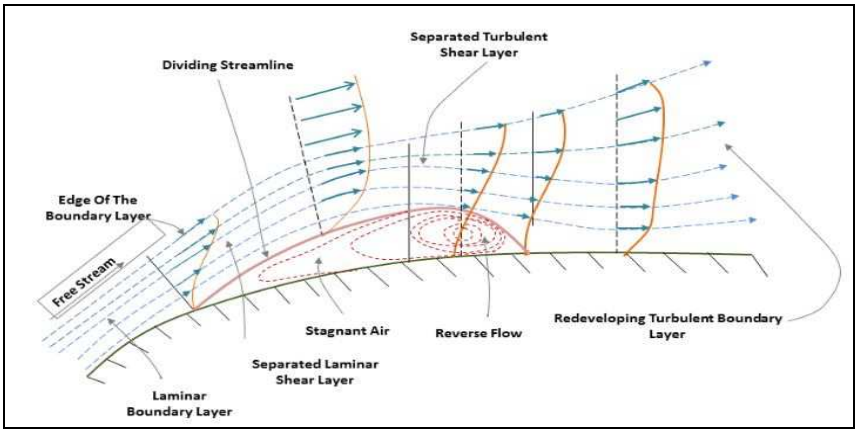

Figure 1.5: Laminar separation bubble

1.2 Lift

Let us now consider a symmetrical airfoil, put into an impulsive motion with velocity –U. Let now assume that its motion starts with a small non-zero angle of attack. If certain conditions of Reynolds number are respected (if Reynolds number is sufficiently high), the boundary layer is thin and the positive and negative vorticity is confined there and in a thin wake. Moreover, for Wu's theorem:

$$\int_V \vec{w} dV = const \qquad (1.11)$$

stating the global conservation of vorticity in a specified volume V. In 1.11 $\vec{w}$ is the vorticity vector, defined as:

$$\vec{w} = \frac{\partial v}{\partial x} - \frac{\partial u}{\partial y} \approx -\frac{\partial u}{\partial y} \qquad (1.12)$$

where *u* and *v* are the velocity component in *x* and *y* direction, considering a body-fixed referred system. In particular clockwise (negative) vorticity is present on the upper surface, while counter-clockwise (positive) is present on the lower surface of the body.

In the case we considered of a non-zero angle of attack, the flow is characterized by two stagnation points that no longer coincide with the leading and trailing edge as was for zero angle of attack. In particular, the front stagnation point A is positioned on the fore part of the lower surface, while the rear one, B, is on the aft part of the upper surface. This situation is presented in picture

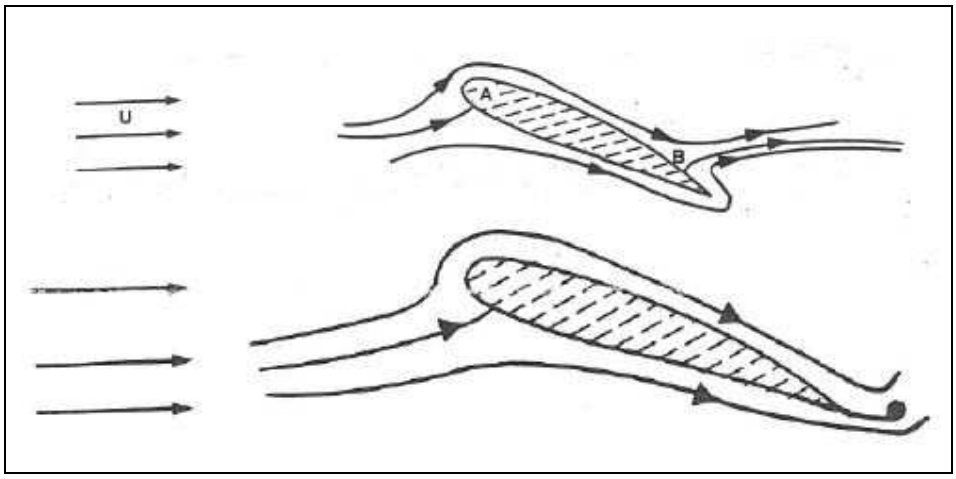

Figure 1.6: Airfoil at $\alpha \neq 0$ at t^- and t^+

The main feature is the streamline rounding the trailing edge, that, doesn't correspond to the actual start of the motion. In fact, the lower boundary layer won't be able to round the trailing edge without separating. This is due to the fact that the trailing edge is characterized by a very sharp edge, and so, the boundary layer experiences a high adverse pressure gradient between the trailing edge and rear stagnation point that leads to separation. After a very fast transient, an amount of positive vorticity is left into the flow downstream, forming what is known as starting vortex. The total strength of the starting vortex is denoted as Γ.

$$\Gamma = \oint_C \vec{V} \cdot d\vec{l} = \int_S \vec{w} \cdot \vec{n} dS \qquad (1.13)$$

If the circuit C we consider includes the airfoil and the wake, the global vorticity, as stated by Wu's theorem, is zero. If we consider in the circuit C the airfoil but not the starting vortex, the global vorticity will be zero no more. In fact, as the global vorticity conservation theorem affirms, if a positive vorticity $+\Gamma$ is left into the starting vortex, it will have a negative vorticity excess equal to $-\Gamma$.

This vorticity will be spread into boundary layer on the airfoil upper surface, and an induced velocity field will be associated to it. This induced velocity field is able to accelerate the flow more on the upper surface rather then on lower. This velocity difference produces, according to Bernoulli's theorem, significantly lower pressure over the upper surface of the airfoil than over the lower one, and thus a lift force, L.

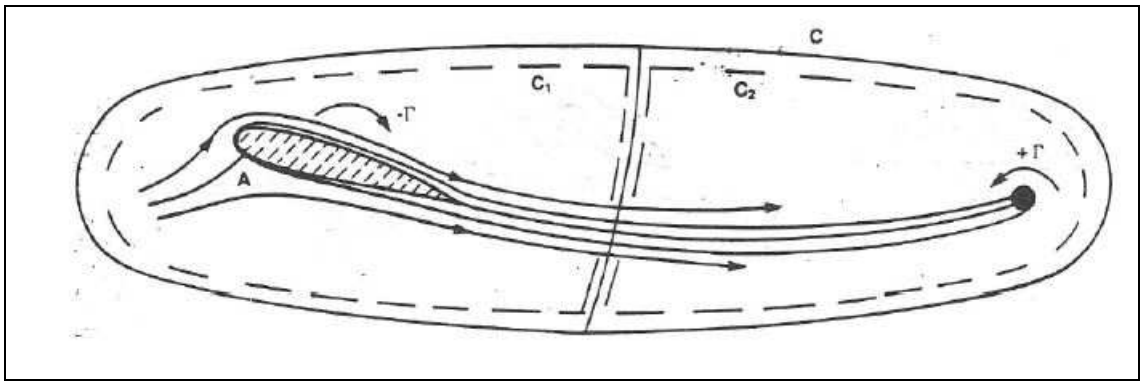

Figure 1.7: Generation of lift

For the global vorticity conservation we can say that:

$$\Gamma_{airfoil}+\Gamma_{wake}+\Gamma_{starting\ vortex}=\Gamma_{tot}=0 \qquad (1.14)$$

With the increasing mutual distance between the airfoil and the starting vortex, the influence of the vortex fades, and the terms $\Gamma_{starting\ vortex}$ becomes negligible. The 1.14 becomes then:

$$\Gamma_{airfoil}= - \Gamma_{wake}$$

With this result, it is finally possible to analyse the problem of a potential flow (since for sufficiently high Reynolds number we can neglect the boundary layer thickness over

the airfoil) around an airfoil with finite circulation and equal to -Γ. The boundary conditions are: impermeability ($\left.\frac{\partial \varphi}{\partial n}\right|_{wall} = 0$)and Kutta condition on stagnation points.

The main result is the Kutta - Joukowski theorem, which establishes a clear link between lift, free stream velocity and circulation over the airfoil:

$$L = -\rho U_{\infty} \Gamma \qquad (1.15)$$

In order to define the lift coefficient, C_l, we shall introduce the pressure coefficient C_p first.

$$C_p = \frac{p - p_{\infty}}{\frac{1}{2}\rho U^2} \qquad (1.16)$$

Since the pressure on the upper and lower surface is different, it is necessary to define both $C_{p,\text{lower surface}}$ and $C_{p,\text{ upper surface}}$.

We can now define the coefficient of lift C_l , where *l* is the bidimensional lift force, integrating over the airfoil chord the difference between the coefficient of pressure of the lower surface and the one of the upper surface.

$$C_l = \frac{1}{c}\int_0^c (C_{p,lowersurface} - C_{p,uppersurface})dx \qquad (1.17)$$

Another definition for the coefficient of lift in a two dimensional way is

$$C_l = \frac{l}{\frac{1}{2}\rho U^2 c} \qquad (1.18)$$

Where ρ is the air density, *U* is the flow velocity and *c* is the airfoil chord.

The trend of the coefficient of lift can be evaluated as a function of the angle of attack α . The diagram for a NACA 0009 is shown in figure 1.8

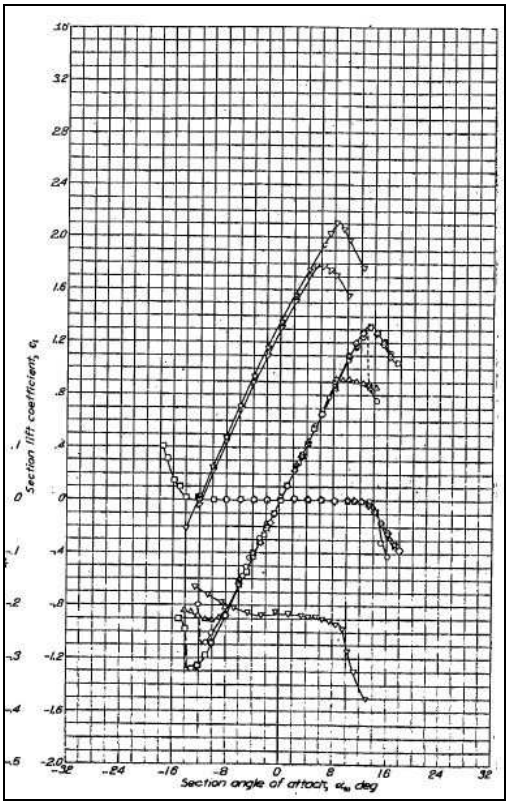

Figure 1. 8: C_l - α diagram of a NACA 0009 for different Reynolds numbers

1.3 Airfoil stall

The stall, in aerodynamics, is a situation where the airfoil reaches its maximum value of lift coefficient, $C_{L,\,max}$. The angle of attack at which this phenomenon occurs is called angle of stall and the airfoil is said to be *stalled*.

The stall condition is deeply linked to the boundary layer separation. In fact, when the angle of attack , α , becomes excessive, the adverse pressure gradient over the upper surface will become so strong that it causes boundary layer separation. As previously said, the lift will reach its maximum value, and then it will start to decrease. This is associated with significant increase of drag and a degradation of the performance characteristics of the airfoil.

Depending on the Reynolds number characterising the flow, and therefore the velocity *U* investing the airfoil, two types of stall can occur: a laminar separation if Reynolds number is low (let's say $Re<5 \times 10^5$), and a turbulent separation for higher Reynolds numbers ($Re>10^7$). The difference between these two kind of separation becomes of key importance in terms of dissipation. In a turbulent boundary layer, in fact, the drag force between the fluid and the surface is greater then in the laminar one. This is due to the remixing of particles in the turbulent flow that causes a higher velocity in the region near the surface, and consequently stronger viscous stresses. So it's clear the advantage in maintaining the boundary layer laminar in terms of fuel saving.
In particular it is possible to distinguish a leading edge stall and a trailing edge stall, depending on the Reynolds number and the thickness of the airfoil considered.

1.3.1 Leading Edge stall

Leading edge stall is typical of airfoil characterized by a thickness-chord ratio of 9-12%. Its main feature is that the airfoil experiences an abrupt and sudden separation of the boundary layer in the region near the leading edge. This behaviour is reflected on the polar having a sharp peak corresponding to the maximum value of lift coefficient, followed by a significant decrease when the stall angle is exceeded.
Since the separation is laminar, leading edge stall phenomenon is accompanied by the generation of a separation bubble on the upper surface.

1.3.2 Trailing Edge stall

This type of stall is a distinguishing feature of the airfoil with a thickness – chord ratio of 15% or above. At high angle of attack, the flow is characterized by a thickening of the turbulent boundary layer on the upper surface. Unlike the leading edge separation, when the angle of attack is increased, flow separation starts at the trailing edge and moves gradually forward as the angle of attack becomes higher. A maximum lift coefficient is reached when the separation reaches the mid – chord point. Beyond this point, the forward progression of the separation continues, creating a much more rounded peak of the polar.

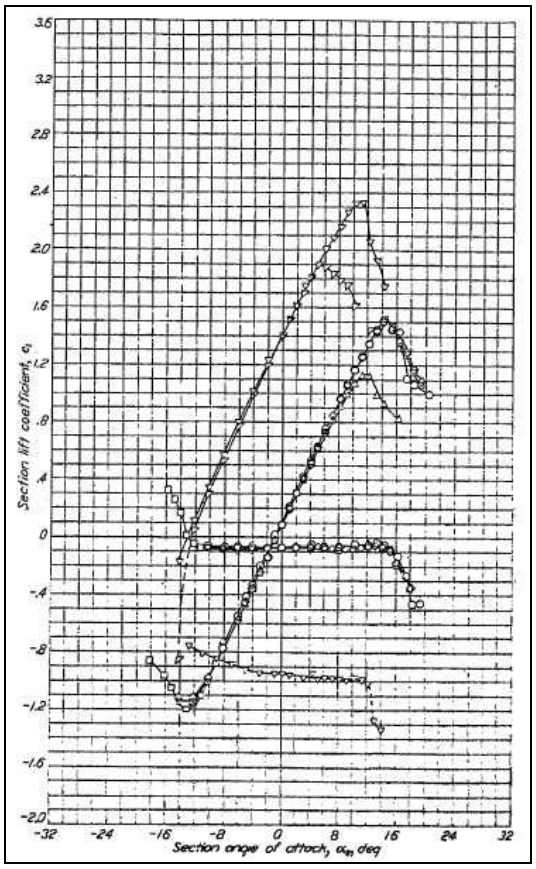

Figure 1. 9: C_l - α diagram of a NACA 0014.
The sharp peak indicates a LE stall

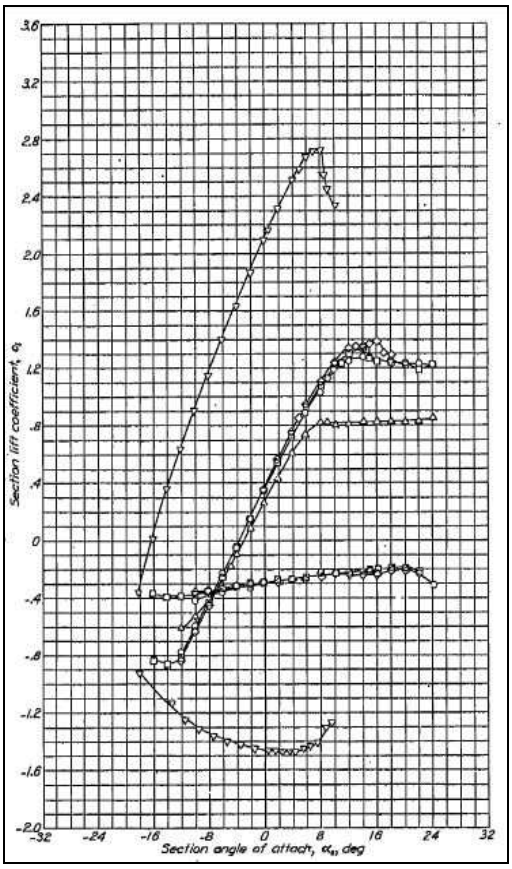

Figure 1. 10: C_l - α of a NACA 4430.
The round peak means a TE stall. The highest curve is the one with the flaps down.

1.3.3 Dynamic stall

The dynamic stall is a non-linear unsteady phenomenon concerning the delay in the stalling characteristics of airfoils that are rapidly pitched beyond the static stall angle. As a result, a higher lift coefficient than the static stall one is achieved, since the flow will remain substantially attached to the surface. This phenomenon often occurs when the airfoil rapidly changes the angle of attack.

The main feature of the dynamic stall is the formation, shedding and downstream convection of a vortex-like disturbance emanating from near the leading edge. The vortex, containing high velocity particles, travels backwards along the airfoil surface. This significantly changes the chord wise pressure distribution over the airfoil, in particular, the lift will be briefly increased. However, when the vortex passes behind the trailing edge, lift reduces dramatically and the normal stall condition is restored.

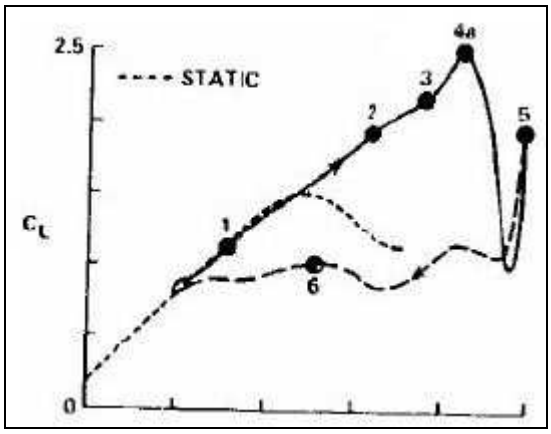

Figure 1. 11: C_l -α diagram comparing static and dynamic stall

1.4 Flow Control Devices

The ability to manipulate and control flow fields is of crucial technological importance in order to enhance efficiency, performances and to achieve environmental compliance. They are often use to delay transition and boundary layer separation.
Classification of flow control devices is based on energy expenditure: active devices require additional power, whereas passive methods don't. As a general rule, when not used, passive devices usually leads to an increase in drag.

1.4.1 Tangential Blowing

Control by tangential blowing is a method often used with trailing edge flap, and it is based on the ejection of a thin high speed jet into the boundary layer. Since separation of the boundary layer is due to the loss of kinetic energy of the particles near the wall, this type of control device is effective because the jet re-energizes the low momentum particles adjacent to the surface. This method exploit the Coanda effect, the tendency of a tangentially blown flow, in contact with a curved surface, to follow the curvature rather than continue travelling in a straight line. The air is usually supplied by the engines, and thanks to a system of pipes and nozzles, is gathered and then blown in the desired points of the upper surface. Tangential blowing can only be used for prevention of separation, unlike the suction that can allow laminar flow control too. Moreover, the flow created by tangential blowing is very sensible to laminar-turbulent transition, so this method often leads to transition.

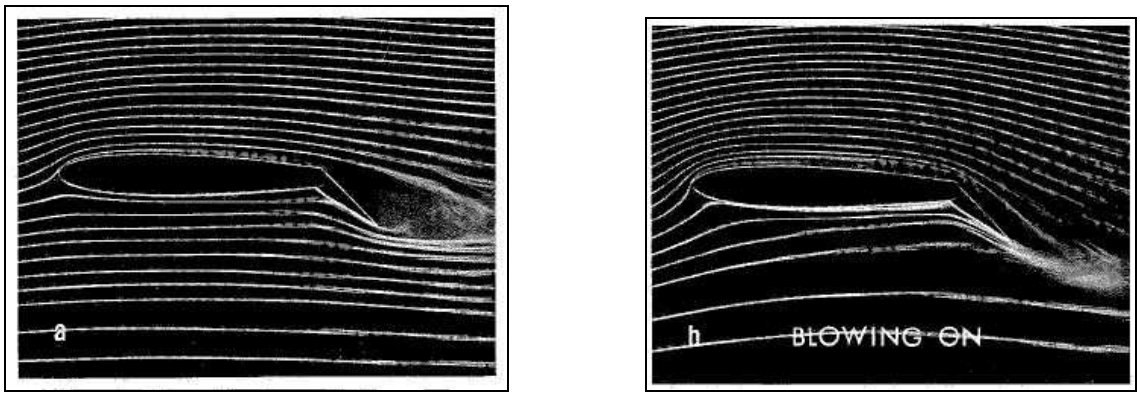

Figure 1. 12 Picture a shows the separation near the trailing edge occurring with blowing off. Picture b shows the reattachment due to the activation of blowing.

1.4.2 Boundary Layer Suction

Boundary layer suction method was first introduced by Prandlt as a one of the means to delay or prevent boundary layer separation. Suction may be applied either through porous surfaces or through a series of finite slots whose aim is to 'suck' inside the body the low momentum particles next to the surface. The result is a much thinner, more stable boundary layer capable of progressing further along the airfoil surface, against the adverse pressure gradient, without separating.

Suction allows, then, to achieve higher lift coefficient, since the separation is suppressed at high angles of attack.

Of practical importance is the necessity to determine the minimum suction fluid necessary. In fact, an excess of suction flow rate, may result in such a power consumption that would make insignificant the power economy gained with the drag reduction.

However, boundary layer suction is not a popular method in production aircraft, since it has some important practical disadvantages. First, it is very sensible to dust blocking the suction holes. Secondly, since the power is provided by the engines, either a failure or an engine blockage would lead to a catastrophe.

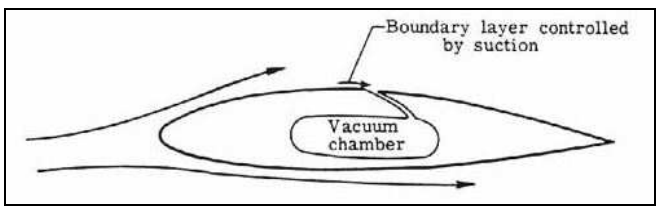

Figure 1.13: Flow control by suction

1.4.3 Vortex Generators

Vortex generators are a typical example of passive flow control device. They are used in order to delay flow separation.

They are typically rectangular, as tall as 80% of the boundary layer and run in span wise lines near the thickest part of the wing. On aircrafts they are installed on the front third of a wing in order to maintain steady airflow over the control surfaces at the trailing edge.

Vortex generators create strong tip vortices which feed high energy air from the external stream to mix with or replace the slower moving air in the boundary layer. Their effect is, then, a reduction of the effect of adverse pressure gradient, delaying or preventing the phenomenon of separation.

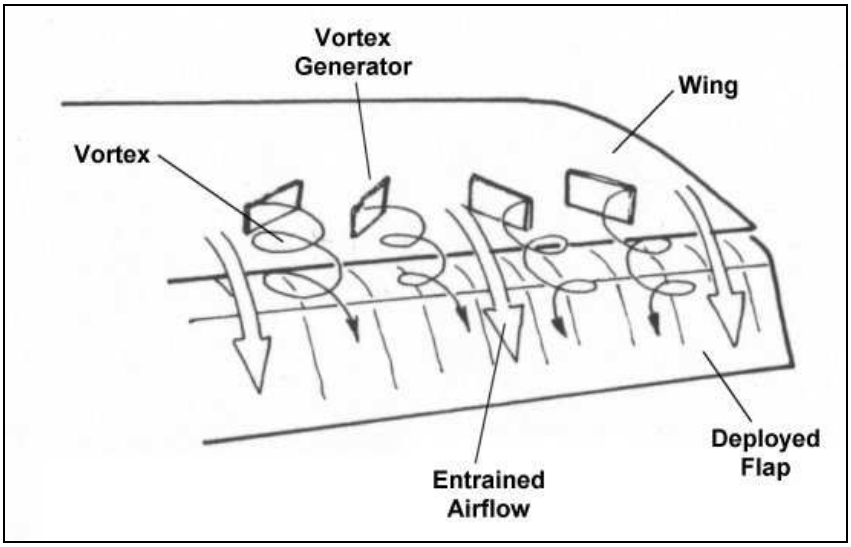

Figure 1.14: Vortex generators over a wing

1.5 Plasma actuators: background and structure

Interest in dielectric barrier discharges (DBD) plasma actuators for flow control has seen a tremendous growth in the past ten years in the US and around the world. This is due to their evident advantages:

- They are fully electronic with no moving parts;
- Fast time response for unsteady applications;
- Very low mass;
- Possibility to install the actuators onto surfaces without needing additional cavities or holes;
- Efficient conversion of the input power without parasitic losses when properly optimised;
- Easy simulation of their effect in numerical flow solvers;

The DBD actuator consists in two metallic electrodes asymmetrically flush-mounted on both sides of a dielectric plate. One electrode is uncoated and exposed and exposed to the air, the other is encapsulated by a dielectric material.
The electrodes are supplied with an AC voltage that, at high enough levels, causes the air over the covered electrode to weakly ionise. The ionised air is plasma, which is why these are referred to as plasma actuators (Cavalieri 1995, Corke & Matlis 200, Corke et al. 2001).

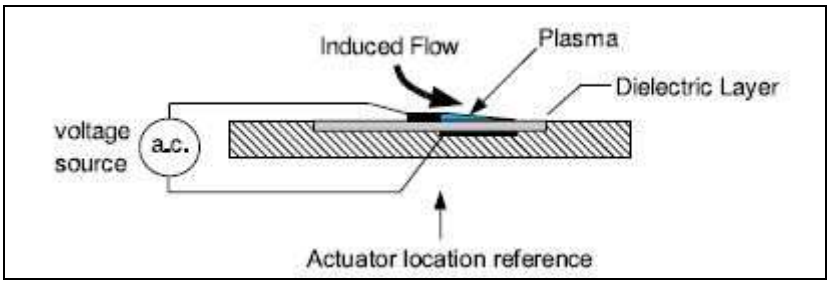

Figure 1.15: Schematic of a single dielectric barrier discharge plasma actuator (Corke et. Al)

To the unaided eye, the ionised air appears blue, usually uniform in colour and distribution. The emission intensity is usually extremely low, requiring a darkened space to view by eye.

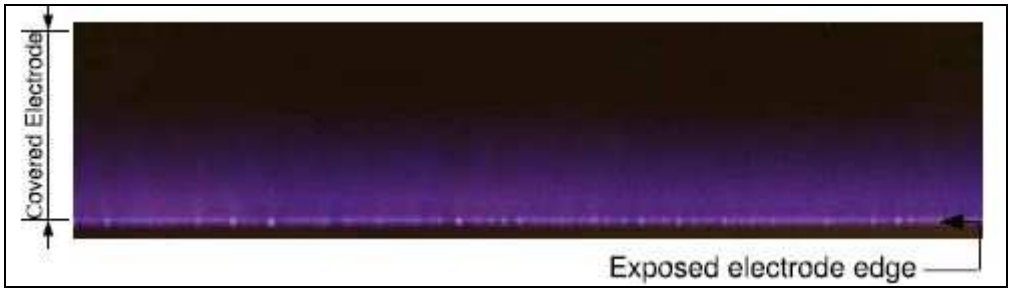

Figure 1.16: photograph of ionized air at 1atm pressure that forms over an electrode covered by a dielectric layer

The mechanism of flow control is through a generated body force vector, resulting from the simultaneous presence of both the ionised air and the electric field, acting on the ambient air (neutrally charged).

In particular, these plasma actuators are based on using the discharge-induced electric wind within the boundary layer to modify its properties and then to actively manipulate the airflow. The aim of using electric wind is in most cases to accelerate the airflow tangentially and very close to the wall, in order to modify the airflow profile within the boundary layer.

1.5.1 Electrical features: working

The word ‘‘plasma’’ was introduced into the physics literature by Langmuir (1926) to denote an electrically neutral region of gas discharge. This definition has in time been broadened and now refers to a system of particles whose collective behaviour is characterized by long-range coulomb interactions (Kunhardt 2000).

A gas discharge is created when an electric field of sufficient amplitude is applied to a volume of gas to generate electron-ion pairs through electron-impact ionisation of the neutral gas (Kunhardt 1980; Kunhardt and Luessen1981; LLewellyn-Jones 1966; Raizer 1991). In order to this to happen, the presence of an initiating number of free electrons is required, either available form the ambient condition or introduced on purpose.

In particular, a traditional arrangement to create a self sustained gas discharge at low pressures of a few Torr or less has involved separated facing electrodes. The electric field established by the two electrodes can either be by direct current (DC) or alternating current (AC). The plasma is generated by increasing the amplitude of the electric field above the breakdown electric field, E_b, which is the value needed to sustain electron-ion

pairs in the gas in the absence of space-charge fields (Kunhardt 1980; Kunhardt and Luessen 1981; LLewellyn-Jones 1966; Raizer 1991).

The minimum of E_b is a function of the driving frequency, and, at atmospheric pressure, is generally lower for an AC input. Once created, the field needed to sustain the plasma, E_s, is lower than E_b and their difference is a function of the operating conditions.

As a result of plasma conductivity a current I flows between the electrodes. Between the plasma and the cathode a region forms: its role is to provide current continuity at this interface. In particular, the current I consists of two components, the conduction current and the displacement current. Their value varies depending on the voltage applied.

When the applied field, electrode cross-section area and static pressure determine a current density, in the boundary region near the cathode, independent from the current flowing in the circuit, a "glowing discharge" is generated. Since the current density scales with the square of the static pressure for constant current, and the cross section area of plasma decreases with increasing pressure at constant current, a particular attention has to be paid. The current density, in fact, increases until the threshold for the development of the instabilities leading to the 'glow to arc' transition, which is a situation that depends on the operating conditions of the discharge.

In general, for aerodynamics applications, for example flow control devices, AC is preferred over DC. This choice is due to the necessity to operate near atmospheric pressure, and thus, the lower breakdown voltage requirement and lack of real current responsible for electrode corrosion effects. In addition to that, it is crucial to consider the actuator's most efficient operating conditions to maximize its effect with respect to input power.

1.5.2 Plasma Actuators Physics

The first important aspect to analyse in the physics behind a plasma actuator, is the mechanism that permits the creation of the discharge, the so called Townsend mechanism.

Let us consider two planes electrodes, between which a dc high voltage is applied in atmospheric pressure air. In the gap, electrons are usually formed by photo ionisation. Under the electric field, established thank to the voltage applied, these electrons are accelerated towards the anode and, by collision with neutral molecules, the ionise the gas. This process can be described as: $A + e^- \rightarrow A^+ + 2e^-$, where A is the neutral particle,

and A^+ is the positive ion. An avalanche develops because of the multiplication of the primary electrons in cascade ionisation. This is the reason why this mechanism is also know as electron avalanche.

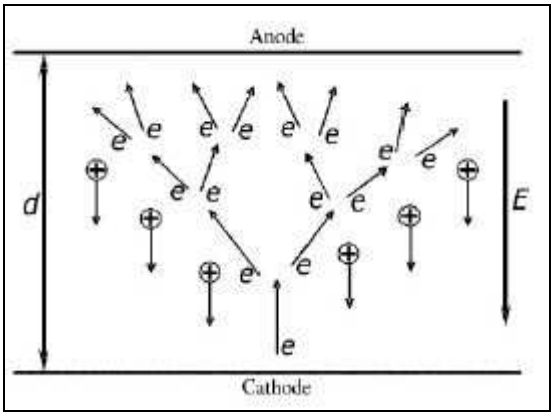

Figure 1.17: Townsend mechanism

Another important aspect of the plasma actuator physics is the manner that it induces flow in the neutral air. The asymmetric electrode configuration results in a flow with a velocity profile similar to that of a wall jet. In one of their paper, Enloe et al. (2004b) correlated the induced reaction thrust acting over the actuator to the applied AC amplitude. A schematic of their experimental set up is shown in figure 1.18.

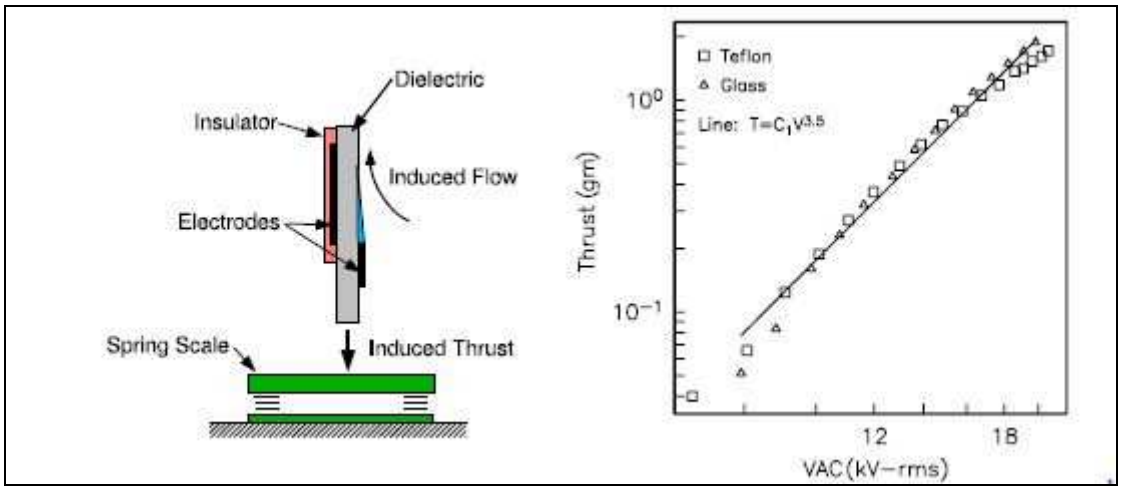

Figure 1. 18: Schematic of experimental set up for measuring induced thrust from SDBD plasma actuator (left) and measured thrust versus applied ac voltage (right) (Corke et. Al)

As shown in figure 1.18, the first measurement of Enloe, indicated that, at lower voltages, the thrust force produced by the actuator was proportional to $V_{ac}^{3.5}$. Post (2004) and

Enloe (2004b), showed that, with increasing AC amplitude, the maximum velocity induced by the actuators was limited by the area of the covered electrode. Thus, the dimension of the dielectric area is of crucial importance, since, if it is too limited, it will be impossible to take full advantage of the applied voltage. This is reflected on the asymptotic trend of the graph in fig. 1.18 at the highest voltages: the thrust no longer increases as $V_{ac}^{3.5}$. Enloe et al. (2004a) also computed the power dissipation in the discharge, which is shown to follow $V_{ac}^{3.5}$, indicating a direct proportionality with the induced velocity.

One of the most efficient methods for predicting the body force field of a plasma actuator, and thus interpret the experimental results, is the space-time lumped-element circuit model developed by Orlov et al.(2006). A schematic of Orlov and colleagues' model is shown:

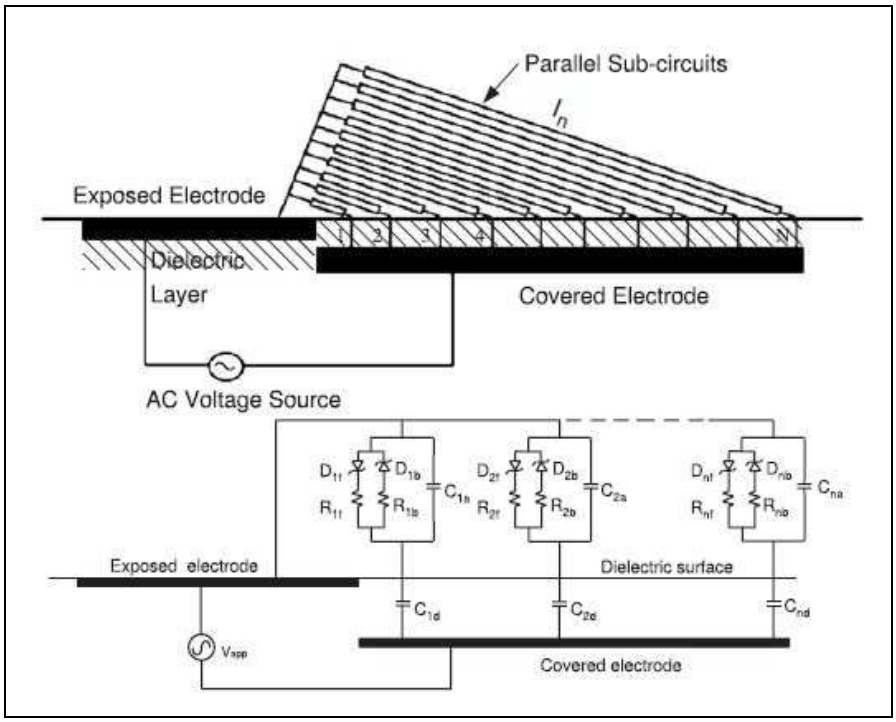

Figure 1. 19: Space-time lumped element circuit model for SDBD plasma actuator. (Corke et. Al)

The distinguishing feature of this model, making it unique from the previous ones, is the division of the domain over the covered electrode into *N* parallel networks, where network 1 is the closest to the surface, and network *N* is the furthest one. Each network consist of an air capacitor, a dielectric capacitor, a plasma resistive element, and has

properties influenced by its distance from the exposed electrode. Zener diodes were shown to be a crucial element to add: they set a threshold voltage level at which the plasma initiates and they switch into the circuit the different plasma-resistance values based on the current direction. The value of the air capacitor, C_{an}, in the n-th sub-circuit is based on its distance from the edge of the exposed electrode. The resistance value in the nth sub-circuit, R_n, is similarly based on its distance from the exposed electrode. The value of the dielectric capacitor for each sub-circuit, C_{dn}, is based on the properties of the dielectric material.

So, for AC applied voltage, the voltage on the surface of the dielectric at the n-th parallel network, $V_n(t)$, is given by:

$$\frac{dV_n(t)}{dt} = \frac{dV_{app}(t)}{dt}\left(\frac{C_{an}}{C_{an}+C_{dn}}\right) + k_n \frac{I_{pn}(t)}{C_{an}+C_{dn}} \qquad (1.19)$$

where k_n represents the diodes, being equal to 1 if the threshold voltage is exceeded. I_{pn} is the time varying current through the plasma resistor defined as:

$$I_{pn}(t) = \frac{1}{R_n}\left[V_{app}(t) - V_n(t)\right] \qquad (1.20)$$

The time dependent extent of the plasma on the surface of the dielectric, *x(t)*, specifies the region where charged particles are present above the covered electrode, defining a moving boundary.

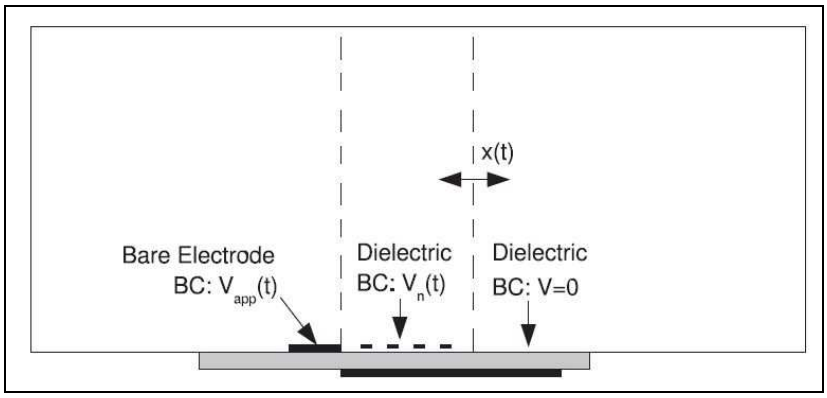

Figure 1. 20: Computational domain for calculation of unsteady plasma body force. BC stands for boundary condition. (Corke et. Al.)

The boundary value of the electric potential on the exposed electrode is $V_{app}(t)$, At the outer boundary, say infinity, the boundary conditions are $\varphi=0$, where φ is the electric potential found in the solution electrostatic Poisson equation and it is used to calculate the time dependent body force produced by the plasma. The result is then:

$$\vec{f}_b(t) = \rho_c \vec{E}(t) = -\left(\frac{\varepsilon_0}{\lambda_D^2}\right)\varphi(t)\vec{E}(t) \qquad (1.21)$$

where λ_D is the Debye length [m] and ε_0 is the permittivity of free space, $8.854 \cdot 10^{-12} C^2 / Nm^2$. Experiments shows that the largest magnitude of the plasma body force is near the edge of the bare electrode closest to the covered electrode, hence at x = 0. From that point, Orlov and colleagues demonstrated that the magnitude decays rapidly over the surface of the dielectric, exponentially.

Overall the model suggested by Orlov and colleagues is one of the most accurate since it allows the plasma boundary conditions to evolve over a timescale short if compared to the AC waveform one. As a consequence, the body force, AC cycle-averaged, scales with $V_{ac}^{3.5}$, which agrees with the experimental data. It also predicts an asymptote in the body force at higher voltages if the covered electrode is too small, as previously said for the experiments carried out. Moreover, as well as being computationally efficient, it allows considerations related to how an actuator might be fielded in a practical system.

1.5.3 Optimisation

The deep understanding of the physics behind the plasma actuators is key to reach a good optimisation of their performances. In particular, in order to do that, some parameters are more important than other to act on.

- AC waveform and frequency: as said before, AC is favoured over DC. Once agreed on that, the best waveform and frequency have to be chosen in order to maximise the body force, and therefore, the plasma effect. As far as what waveform concerns, experiments have shown that a sawtooth form is the best. Since the ionisation occurs as long as the difference between the instantaneous AC potential and the charge build up on the dielectric exceed a threshold value, the sawtooth is the waveform that, experimentally, best verify this condition. The

choice of the AC frequency is based on the actuator capacitance, as Orlov and colleagues (2006) indicated. Figure 1.21 shows the dependency between thrust and V_{ac}, with each curve corresponding to a different frequency. In general, at fixed power, if the current is too large, the applied voltage will decrease and the body force too.

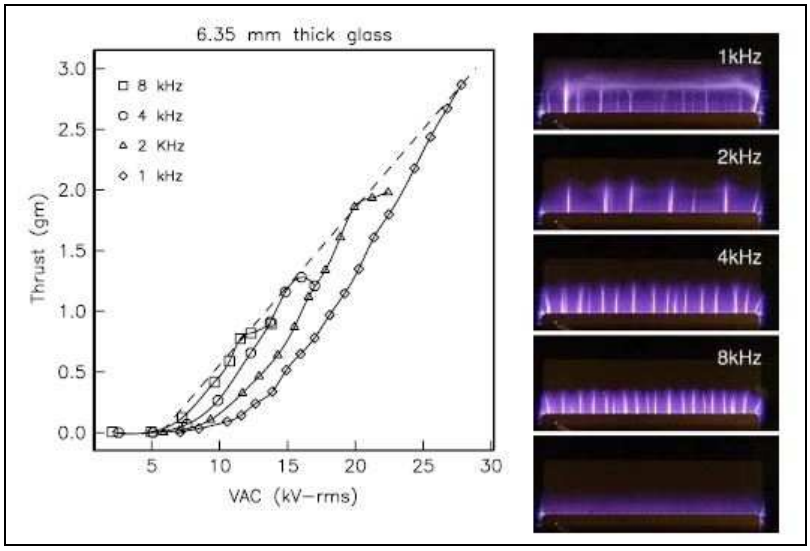

Figure 1.21: Induced thrust from a SDBD plasma actuator for a 6.35 mm thick glass dielectric for different AC frequencies of the applied voltage (left). Corresponding images of plasma for each frequency at maximum thrust.(Corke at. Al)

- Geometry: experiments of Forte et al. (2006) demonstrated the influence of the amount of overlap between the bare and the coated electrode in an asymmetric configuration. They designated the gap space g and L_{ce} the length of the covered electrode. Their results indicated that for $\frac{g}{L_{ce}} \geq 2$, plasma effectiveness rapidly drops off.

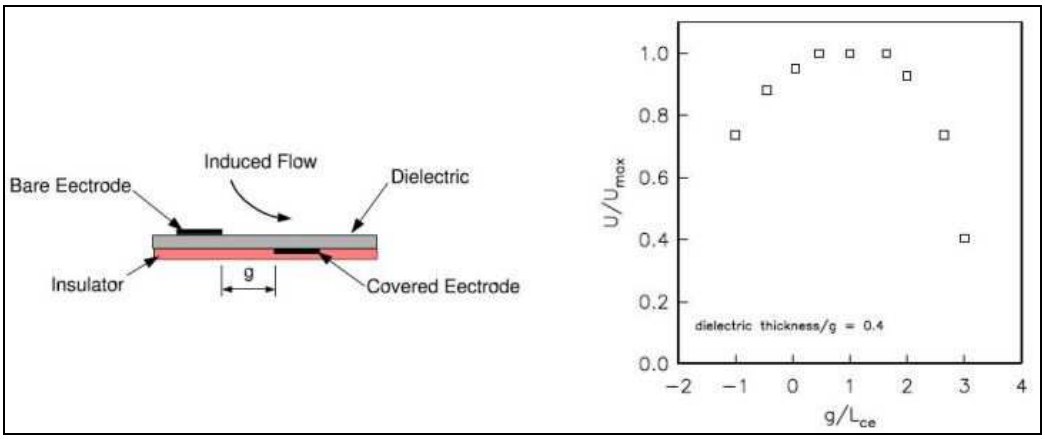

Figure 1.22: Effect of gap spacing between bare and covered electrodes on maximum induced velocity in still air. Re plotted data form Forte et al. (right). (Corke at. Al)

- Dielectric thickness: in the choice of the thickness of the dielectrics two main aspects have to be considered. The first is the breakdown voltage per thickness, the second one the dielectric coefficient, ε . To guarantee that the dielectric won't break down at the applied voltage, a minimum thickness has to be fixed. Usually this can be accomplished with only a fraction of millimetres. If the dielectric coefficient is low, recent experiments have shown the benefit in using thicker dielectrics. Another advantage deriving from thick dielectrics is the lowering of capacitance, since it is proportional to ε /h, where h is the dielectric thickness. This has important consequences. Lowering the capacitance, lowers the power loss through the dielectric, which is otherwise manifest in heating, and allows higher voltages to be reached. Higher voltages means stronger body force.

1.5.4 Aerodynamics effects and application

Among the active flow control techniques, the use of plasma actuators has been demonstrated to be effective in several applications, including flow separation and boundary layer control. This aspect of particular interest, since it could lead to a lift control without flaps for instance.

It was only by the end of the 1990s that DBDs specifically constructed for aerodynamics flow control applications appeared in literature, and the number of the applications is ever growing. From that time on, there has been an increasing interest and research projects concentrated on DBDs, both experimental and numerical, flourished worldwide.

Most of the opinions on the applicability of DBDs agree on their significant effect on boundary layer only at low Reynolds number flows.

This lack of effectiveness for higher free stream speeds, suggests Chernyshev, is based more on the low energy input to the air flow, rather than a reduction in the output ion wind due to electric field dampening.

However, the effectiveness of plasma actuators in controlling flow separation has been demonstrated by several researchers, and one of the most important experiment is the one carried out by Corke at al. (2003). Their tests were concentrated on demonstrating measurable lift enhancement for a full range of angles of attack, both in steady and unsteady actuations, using a NACA 0015. The results obtained with the steady actuation are shown:

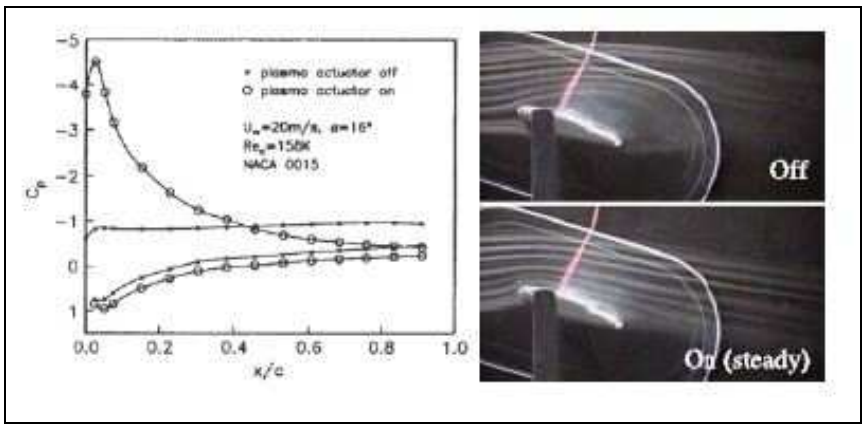

Figure 1. 23: coefficient of pressure distribution with plasma actuator on and off, for α =16° and Re=158000 (left). Visualisation of the streamlines along a 12° inclined NACA 0015 with and without actuation (right). (Corke et. Al)

In particular, this actuation induces a pressure recovery near the leading edge and moreover, the values of the lift coefficient with the actuators turned on, are constantly higher than the post stall condition with actuators off.

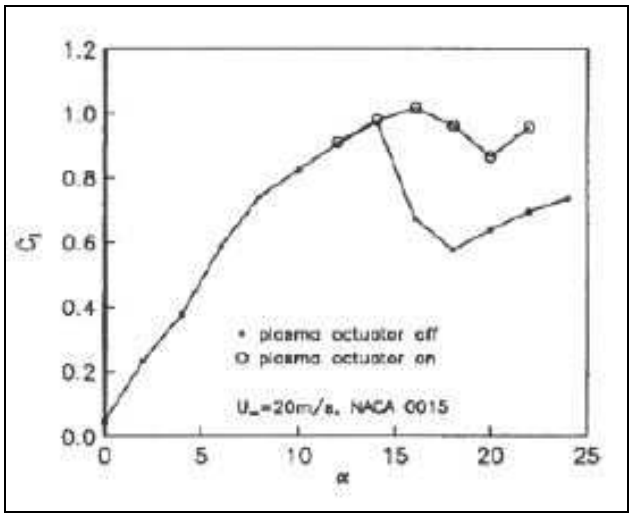

Figure 1. 24: Comparison of computed lift coefficient with plasma on and off at U= 20 m/s and Re=158000**.** (Corke et. Al)

Corke at al. investigated even the effects of the unsteady actuation, placing one actuator at the leading edge and one at the trailing edge. The results (1.25), clearly shows that the effect of the actuator on separation prevention is enhanced when the actuator is impulsively cycled. The unsteady actuation then allows to maintain the flow attached up to 9° past after the normal stall angle.

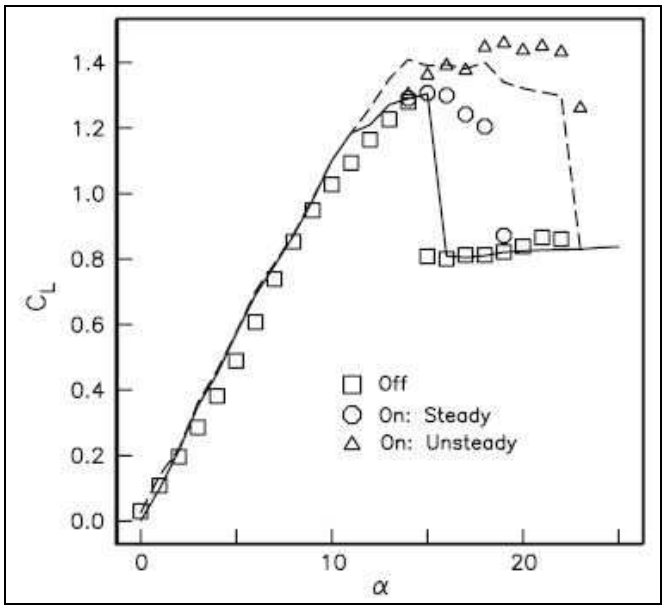

Figure 1. 25: Lift coefficient versus angle of attack with leading edge actuator off and on at optimum unsteady frequency. (Corke et. Al)

It's important to highlight another crucial result: most efficient results for an unsteady actuation frequency corresponding to a Strouhal number equal to 1, where the Strouhal number is defined as:

$$St = \frac{fL_{ref}}{U_{ref}} \qquad (1.22)$$

Where f is the frequency of vortex leaving the airfoil, L_{ref} the reference length and U_{ref} is the reference velocity.

CHAPTER 2

EXPERIMENTAL SET UP

In this chapter we are talking about the experimental set up needed to carry out our experiment. In particular we are describing the wind tunnel of the Applied Aerodynamics Laboratory in Forlì, the airfoil and the fluid dynamics system to measure the influence of the actuators on the flow. We are then explaining the electrical set up, namely the actuators and the powering system.

2.1 The wind tunnel of the Applied Aerodynamics Laboratory

The wind tunnel of the Laboratory is an open loop and suction type and it is 15 metres long (fig 2.1). The test section is 600 mm large, 900 mm high and 1800 mm long with a 6.9 contract ratio. The value of the velocity inside the test section is obtained through a Prandlt probe measuring the static pressure and total pressure. The maximum velocity reachable is 50 m/s. The fan located at the drive section, is powered by a 30kW asynchronous motor, frequency controlled through an inverter.

2.2 Force measurements: Six component balance

The airflow over the model results in aerodynamic forces and moments measured then by the balance (fig. 2.2). It is characterized by: (table 2.1)

	Full Scale Input	Full Scale Output	Sensitivity
X axis forces	350 N	+/- 2500 mV	0.5 g/logic level
Y axis forces	700 N	+/- 2500 mV	1.63 g/ logic level
Z axis forces	300 N	+/- 2500 mV	0.65 g/ logic level
X,Y,Z axis moment	100 Nm	+/- 2500 mV	0.15 g m/ logic level

Table 2.1: six-component balance characteristics

The balance is then connected to the NI USB6221 board to acquire data and store them in a PC.

Figure 2.1: Fan

Figure 2.2: Six component balance

2.3 Prandlt tube and pressure transducers

To measure mean flow velocity, a Prandlt tube was used, linked to a Setra capacitive transducer with a full scale equal to 0-15 inches WC and a full scale output of 0-5 V DC.

The Setra transducer (fig 2.3) is connected to a NI USB6221 board, which converts the data received into analogue, and then it transmits the output to a PC for the data acquisition and analysis.

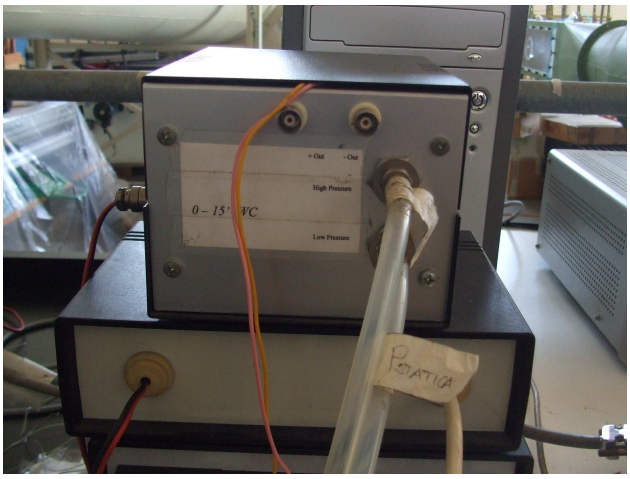

Figure 2.3: Setra pressure transducer

A Prandlt tube (fig. 2.4) hosts a static and a total pressure hole. The total pressure port is located tangentially to the stream, to the front edge of the probe, and, through transducers, it gives the total pressure p_o. The static pressure port is placed on the pipe body, normal to the flow, and it gives the static pressure measurements, p_s. The difference between the total and the static pressure, supposing the flow as isentropic, results in the dynamic pressure:

$$p_o - p_s = p_d \qquad (2.1)$$

In order to calculate the velocity in the most precise way possible, taking into account that air density can change depending on the room temperature and pressure, that can vary quite frequently, we elaborated a VI using LabView™.
The inputs given to the VI were: the dynamic pressure supplied by the NIUSB board connected to the Setra, the room temperature [K] and pressure [Pa]. We can then deduce air density, considering a dry air environment, through the ideal gas law:

$$Pv = nRT \qquad (2.2)$$

Obtaining:

$$\rho = \frac{p_{atm}}{T_{room} \cdot R} \qquad (2.3)$$

Where p_{atm} is the atmospheric pressure measured in the room, T_{room} is the room temperature and R is the gas constant, whose value for dry air is 287.058 J/kgK.

Then, applying Bernoulli's theorem:

$$p_d = \frac{1}{2}\rho U^2 \qquad (2.4)$$

It's possible to calculate the velocity inside the wind tunnel:

$$U = \sqrt{\frac{2p_d}{\rho}} \qquad (2.5)$$

Figure 2.4: Pitot Tube

2.4 Board NI USB 6221

This board (FIG. 2.5) allows us to acquire, through a computer, data from the balance and from the pressure transducer. The board NI USB 6221 has a multifunctional I/O system, with a digital USB I/O system, that let us sample up to 250 kS/s.
The process of digitalisation is on 2^{16} levels, since it is a 16 bit board.
In particular, if we connect the board to the pressure transducer, since it has a full scale input of +/-5V, the appreciable levels are 0.0000763. The sensitivity of the board is then, of 0.0763 mV per level.

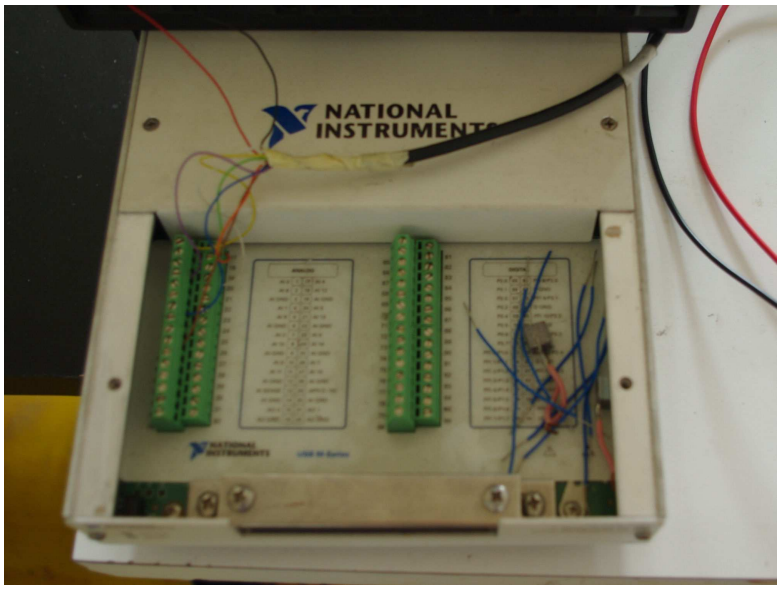

Figure 2. 5: Board NI USB6221

2.5 Step Motor

Step motor (fig 2.6) synchronous, powered by DC, brushless, it is capable of dividing its rotation in steps. In particular, in the one available in the AA Laboratory, each step corresponds to a 0.024° rotation.
The model used is a 5 phase motor, powered by a 1.4 A current and 0.57 V.

Figure 2. 6: Step motor

2.6 The Airfoil model

In order to carry out our experiment and test the effectiveness of the plasma actuators, a NACA 0015 airfoil was chosen. This particular choice is mainly due to the fact that this specific airfoil is one of the most used for experiments. Moreover, other research groups carried out tests on similar airfoil, such as NACA 0012 and NACA 23012, and comparing the results they obtained with ours turned out to be useful.

The NACA 0015 airfoil is symmetrical, as 00 means it has no camber. As for its thickness, 15 indicates that the airfoil has a 15% thickness to chord length ratio. We can see a picture in fig. 2.7:

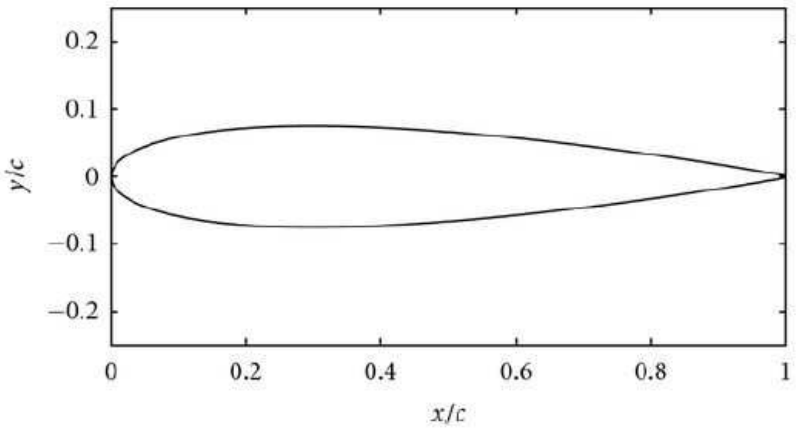

Figure 2. 7: NACA 0015

In first place, once we had put the airfoil inside the test section of the wind tunnel, we characterized it. In figures 2.8 is presented the C_L-α diagram where the trend of C_L with angle of attack is shown for different velocities. In particular, the velocities indicated are the ones used to test the plasma actuator effectiveness.

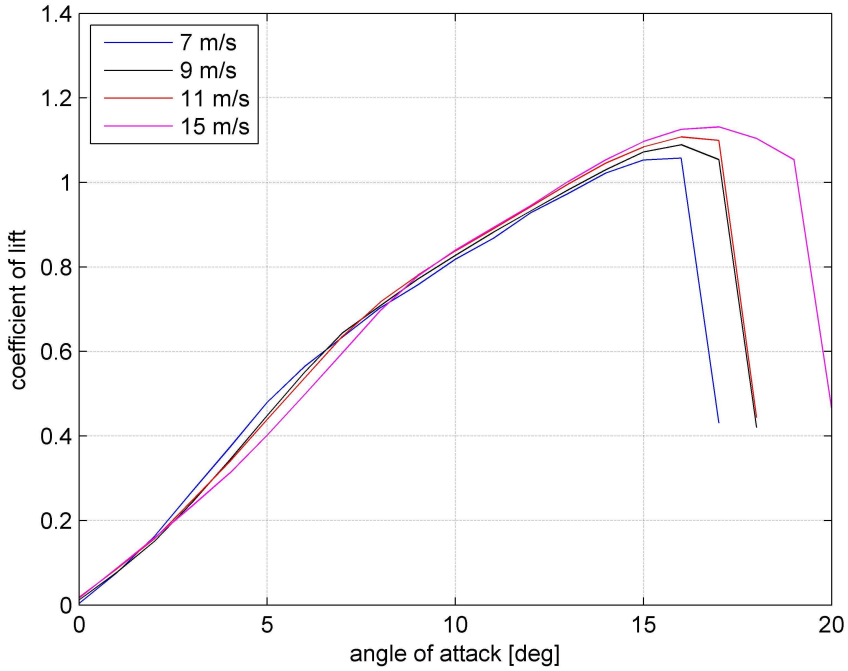

Figure 2. 8: C_L-α diagram

Through MIT Xfoil freeware software it is possible to analyze aerodynamics characteristic features of the airfoil, supposing a viscid flow with $Re=3.21 \cdot 10^5$, Mach number M=0.043, a temperature of 25°C and a velocity of 15 m/s. Results obtained are shown in fig. 2.9. Solid lines represents the viscid case, the dotted one the inviscid case. From a first analysis of fig. 2.10, at α=15° a boundary layer transition is visible at 0.044c, where c in the airfoil chord length.

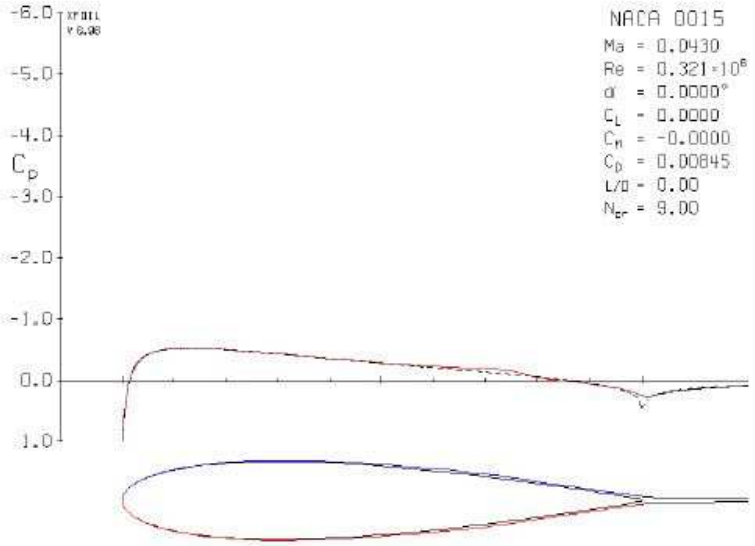

Figure 2.9: NACA 0015 C_p diagram at α=0° [image from Montecchia thesis (2012)]

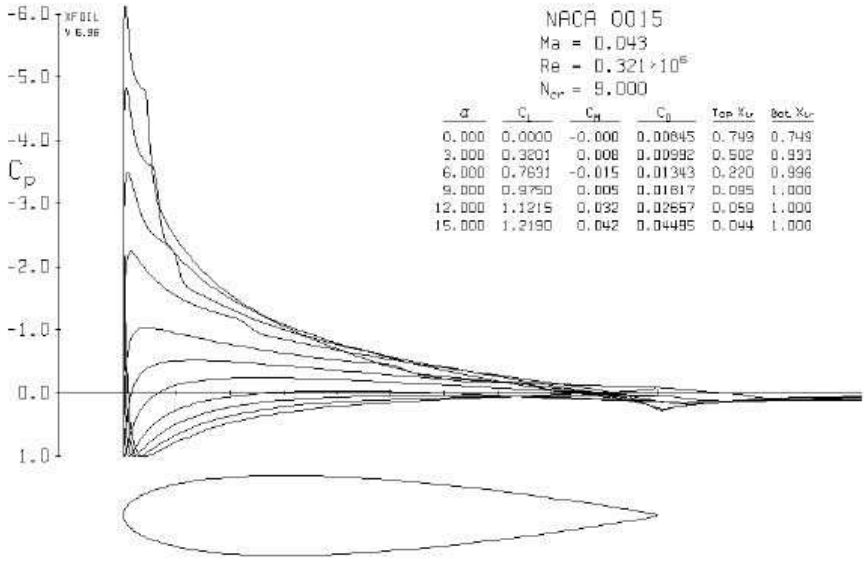

Figure 2. 10: NACA 0015 C diagram from α=0° to α=15° [image from Montecchia thesis (2012)]

In order to allow the flow to be as bidimensional as possible, two transparent and matt plates were installed normally to the wing surface. This reduces three-dimensional edge effects, that can badly influence our results. The final configuration is shown:

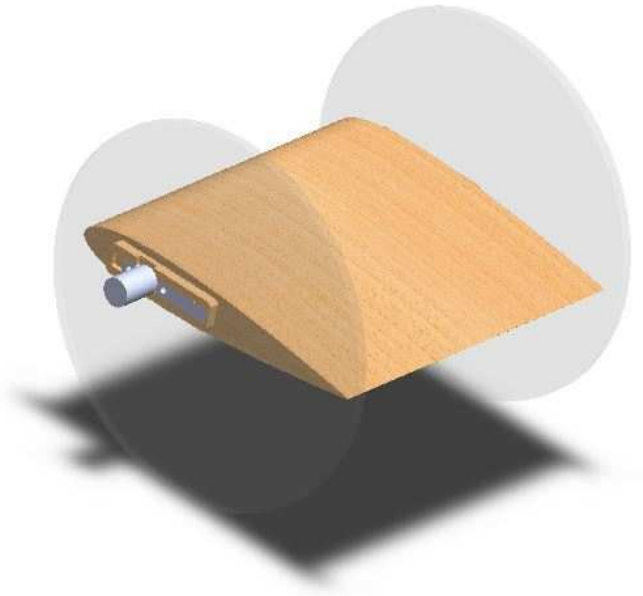

Figure 2. 11: Final configuration

2.7 Actuators set

2.7.1 Plasma actuators

The aerodynamics application of plasma actuator required specific conditions to be verified. In particular, the actuators should be reliable and have high aerodynamics performance, and therefore, they should be thin. On the other hand, to make assembly on the airfoil easier, actuators should be flexible.

This last condition has revealed to be particularly binding. Firstly, in fact, the dielectric chosen was in Teflon material. It has very advantageous features: it is an insulator able to reach excellent aerodynamics performances even with low thickness, it is resistant to high temperature (until 200°C) and it has good electrical characteristics too (an electrical rigidity of 65 kV/mm and a dielectric constant ε_r=2.1)

Despite that, its thickness of 1-2 mm doesn't guarantee a sufficient flexibility, and so Teflon had to be replaced by Kapton.

Kapton is a polyamide film developed by DuPont, which can remain stable in a wide range of temperatures (from –269°C to 400°C). Its good dielectric qualities (ε_r=3.4), together with its light weight and flexibility, have made it a favourite material in our application.

Nevertheless, Kapton is available only in thin sheets, with a thickness smaller than the needed, about 1-2 mm, and this involves slightly worse aerodynamics performances than the ones obtained with Teflon. However, to reach a thickness suitable with working voltages , one solution was to juxtapose six layers of Kapton. Yet, this solution have some important disadvantages on the practical side:

- Complexity in the realization;
- Possible generation of air bubbles that would degrade the electrical properties of the insulator.

This is why the final dielectric configuration (fig. 2.12) features a sheet of Mylar (250μm thick) between two layers of Kapton (90 μm thick). In particular, to keep down increasing effect due to electrodes' edges, it was necessary to guarantee a superimposition of 1mm between electrodes (fig. 2.13). The characteristics of both Kapton and Mylar are shown in table 2.2 and table 2.3 respectively.

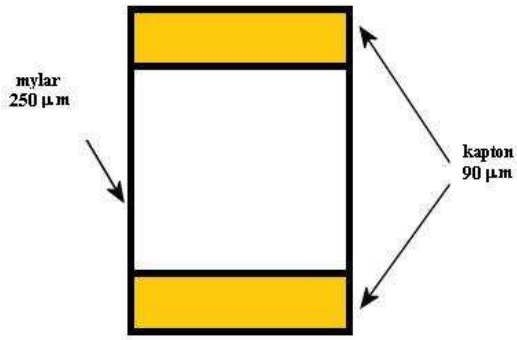

Figure 2. 12:schematic of final dielectric configuration

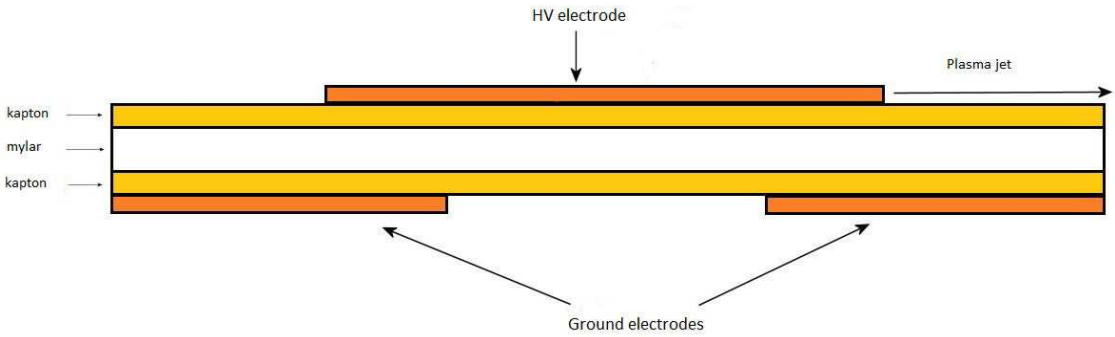

Figure 2. 13: schematic of final electrodes configuration

Properties	Unit of measurements	Values	Test Method
Density	g/cm^3	1.42	ASTM 1505
Ultimate strength	kg/cm^2	1750	ASTM-D 882
Ultimate extension	%	70	ASTM-D 882
Thermal conductivity	W/mK	0.15	DuPont Test
Flammability		94 v-0	UL 94
Dielectric rigidity	kV/mm	280	ASTM-D 149
Dielectric constant		3.4	ASTM-D 149
NaOH (10%) resistant		Degrades	1 year at 23°C
Transformer resistant to oil		Excellent	1 year at 23°C
Kapton thickness	µm	60	
Silicon glue thickness	µm	25	

Table 2.2: Kapton features

Properties	Unit of measurements	Values
Thickness	µm	250
Sheet density	g/cm^3	313
Ultimate strength	kg/cm^2	1750
Dielectric rigidity at 25°C	kV/mm	70-150

Table 2.3: Mylar features

2.7.2 Preliminary plasma actuators tests

Before starting with the assembly of the set on the airfoil, electrical tests had been done on two actuators to find the best power conditions.

The couple realized was 330 mm long, enough to cover all the airfoil span wise.

Actuators are asked to be continuously functional for at least 10 seconds, without discharges occurring, and to keep aerodynamics performances unchanged.

Supplying the actuators with 8.5 kVp 10Hz, they will damage within one minute. During the testing process, then, a voltage of 7 kVp 10Hz had been chosen, in order to make sure actuators are continuously functional for over one minute.

Since our aim was to make plasma vectoring possible, the power conditions changes depending on how many actuators have to be powered. In case of just one actuator working, power value is about 30 W, whilst, it increases to 55-60 W when two actuators are required.

2.7.3 Actuators assembly

Once concluded preliminary test, a 8-actuator set was put on the airfoil, both on the upper and lower surface. Figure 2.14 presents a schematic of the final assembly.

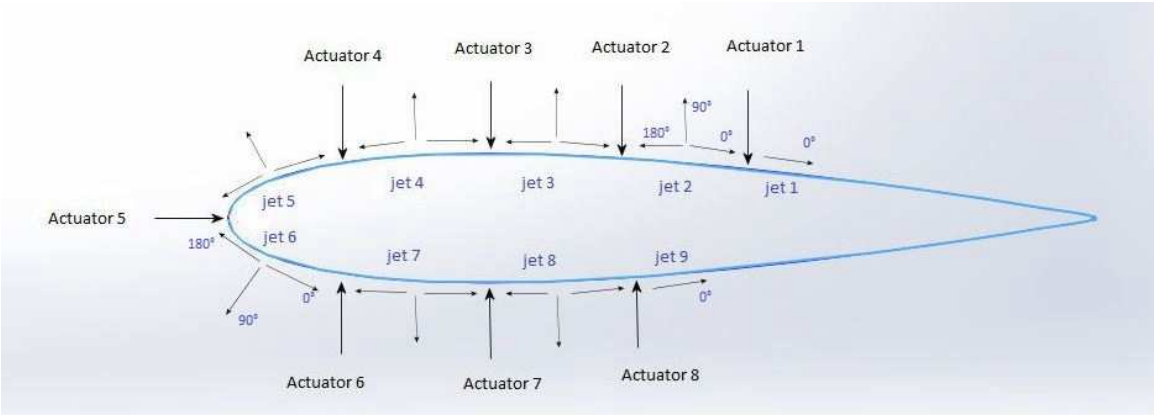

Figure 2.14: schematic of final assembly

This configuration, consisting of one electrode supplied whit high voltage and two grounded, let us achieve plasma jet vectoring.

A jet of plasma will form in between two adjacent actuators. Depending on the voltage applied, the jet can be differently oriented, as schematised in fig. 2.15. A Schlieren image of a plasma jet in steady actuation is presented in fig. 2.16.

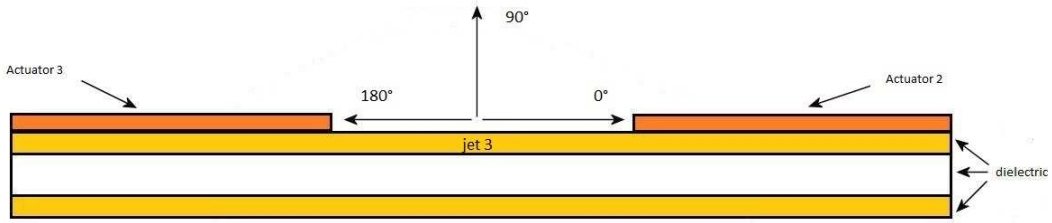

Figure 2.15: Schematic of oriented jet.

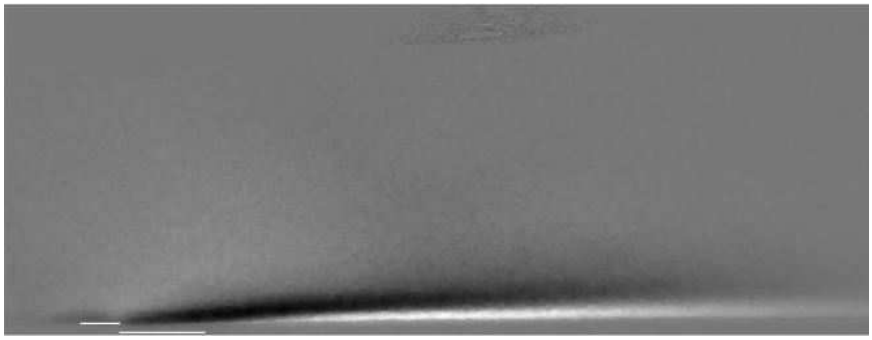

Figure 2.16: Schlieren photography of a plasma jet in steady actuation

Let us consider, for instance, jet 3:

- 0° jet is obtained by powering only actuator 3, whilst 180°, only by powering actuator 2.
- 90° jet will form supplying with the same AC voltage both actuators 2 and 3.
- Intermediate angles jet is possible by powering both actuator 2 and 3 with different values of AC voltage.

Actuators have been installed on the airfoil through acrylic glue (Adhesive Transfer Tape 3Mc), 25 μm thick, able to resist a temperature of 120°C.

Grounded electrodes have been short-circuited while high-voltage ones have been separated in order to power actuators one by one. The final result is presented below:

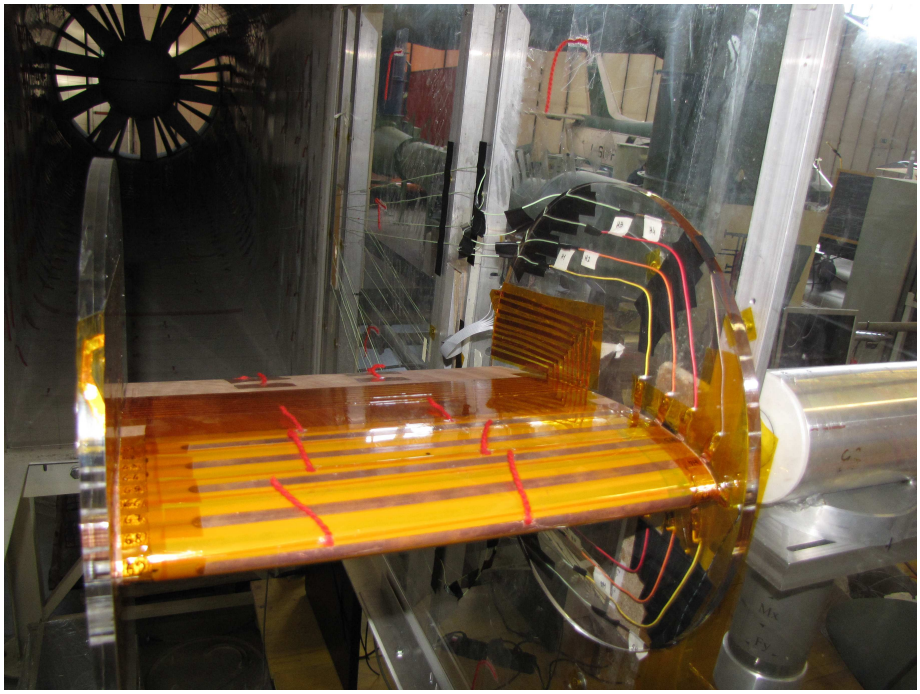

Figure 2.17: Upper surface final configuration

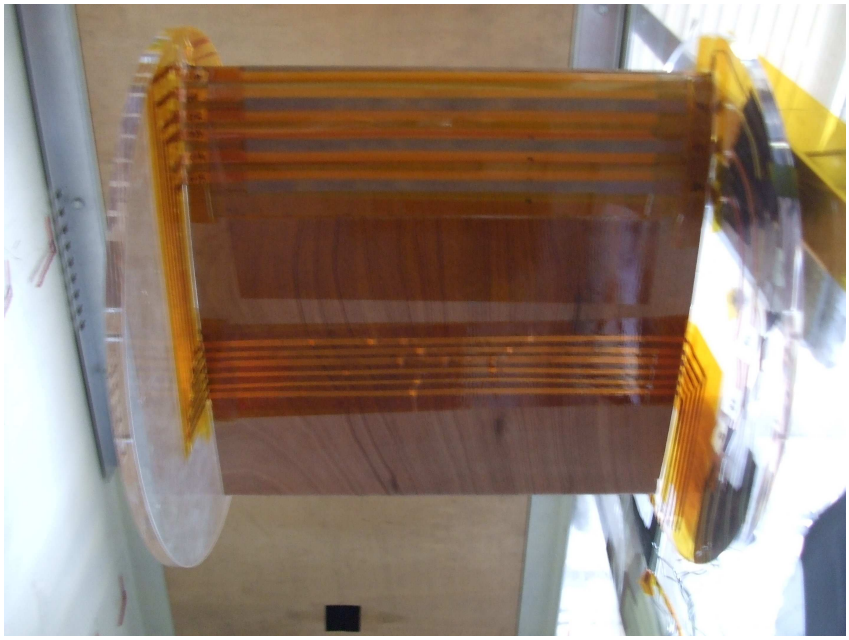

Figure 2.18: Lower surface final configuration

2.8 Minipuls

Actuators powering is ensured by a high voltages and frequencies sinusoidal generator. In our experiment we used Minipuls2, by Electrofluid Systems. (fig. 2.19)

Figure 2.19 MinipulsII

It requires a sinusoidal reference signal and a DC input, which is modulated by two mosfet transistor. The modulated DC voltage is then sent to the first of the five ferrite transformers.

After this transformer the voltage is given by:

$$V_{out} = 2V_{in} + \left(\frac{N_1}{N_0}\right)V_{in} \qquad (2.6)$$

The transformers are linked in series in order to reach the voltage needed, which will result from summing the out voltages of each transformer.

The generator is a resonant one, it is then required to modify the matching transformer inductance so that it is compatible with the capacitive load.

The detailed characteristics of Minipuls2 are gathered in Table 2.4 below.

Feature	Unit of measurements	Value
Input voltage	V	15-40
Input power	W	110
Input power for a bounded time	W	160
Maximum output voltage (idle, 14 kHz)	kV_{pp}	24
Frequency	kHz	5-30
Temperature	°C	0-40

Table 2.4: MinipulsII features

2.9 Wind Tunnel Set Up

Once the actuator set had been put on the upper and lower surface, the airfoil can be installed into the test section of the wind tunnel as shown in fig 2.20:

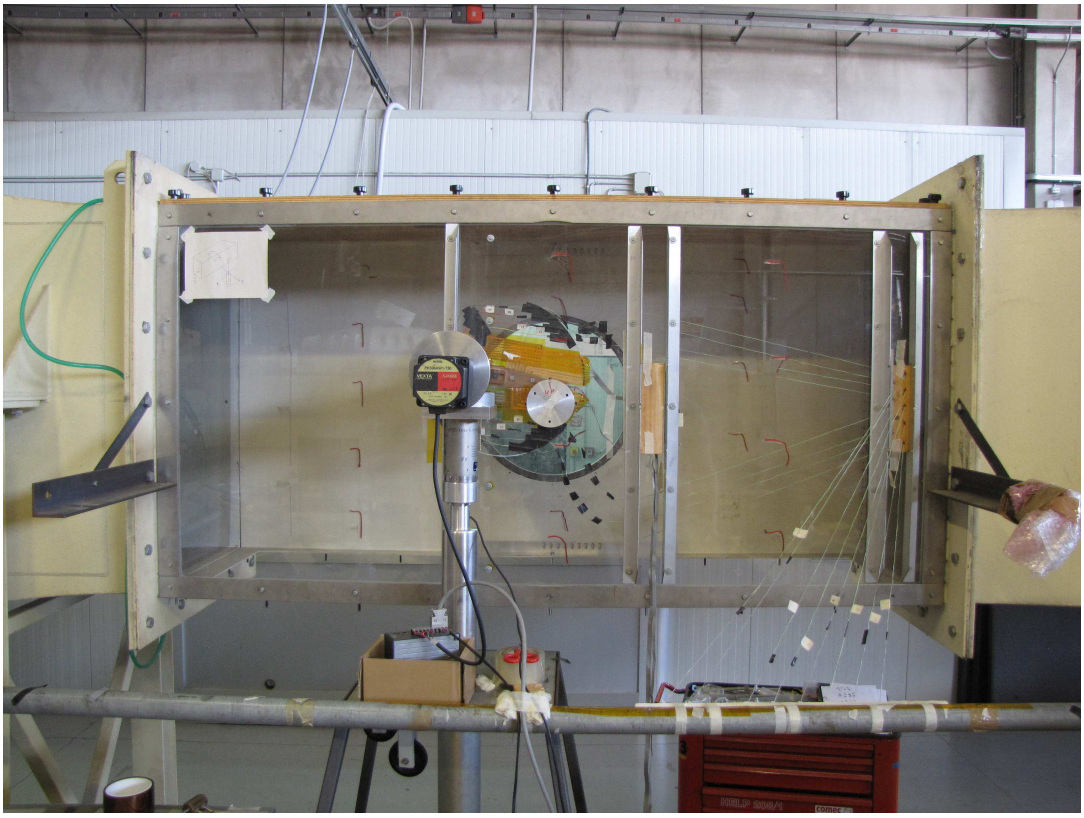

Figure 2.20: Wind tunnel final set up

In order to get results for different angles of attack, the airfoil is connected to the step motor allowing the control of the variation of the angle with a computer. This method has the advantage to be more precise than the manual procedure through a goniometer. The rotation is made possible by a shaft, connecting airfoil and motor (fig. 2.21).

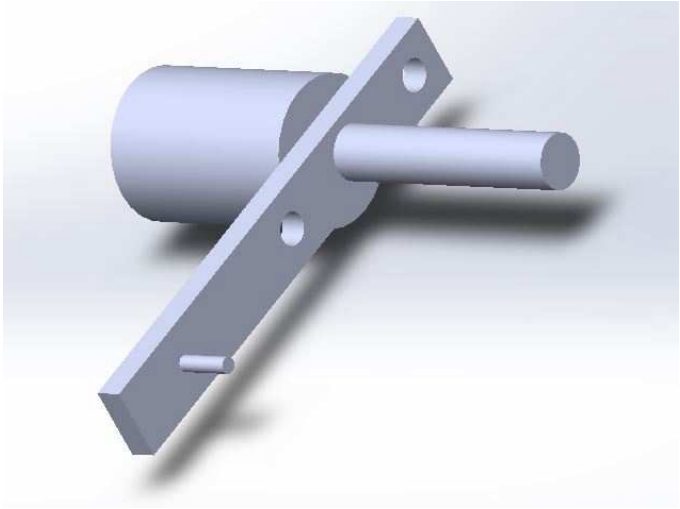

Figure 2.21: Shaft

Since the airfoil is not as large as the test section, carrying out the cables without interfering with lift measurements was difficult. Therefore, the solution was to make wires pass onto the surface of the airfoil. Two extra strips had been added near the trailing edge in order to make it possible.

CHAPTER 3

EXPERIMENTAL RESULTS ANALYSIS

In this chapter we are presenting and analysing the data obtained from our experiment. In particular we are going to focus on lift coefficient variation depending on the Reynolds number and, of course, actuators‘ effectiveness.

Measurements have been done at different angles of attack, different velocities, turning on one or two actuators, both in steady (where frequency of signal repetition is zero) and unsteady actuation. In particular, the range of frequencies varies from 5Hz up until, in certain cases, 70 Hz. As for the duty cycle, defined as the ratio of the duration of the event to the total period of a signal, is of 50%. Duty cycle is important because it allows us to define the duration of actuator’s powering, and therefore, to control the energy we supply. The choice of the unsteady carrier is influenced by the Strouhal number:

$$St = \frac{fL}{v} \qquad (3.1)$$

Where f is the frequency of vortex shedding, L is a characteristic length of the body we are considering, and v is the flow velocity. In particular the unsteady carrier is chosen to reach St=1.

In general, the evolution of the plasma jet in time is depicted in fig. 3.1, where the first three images represent the transient, while the last one on the right side is the final steady situation.

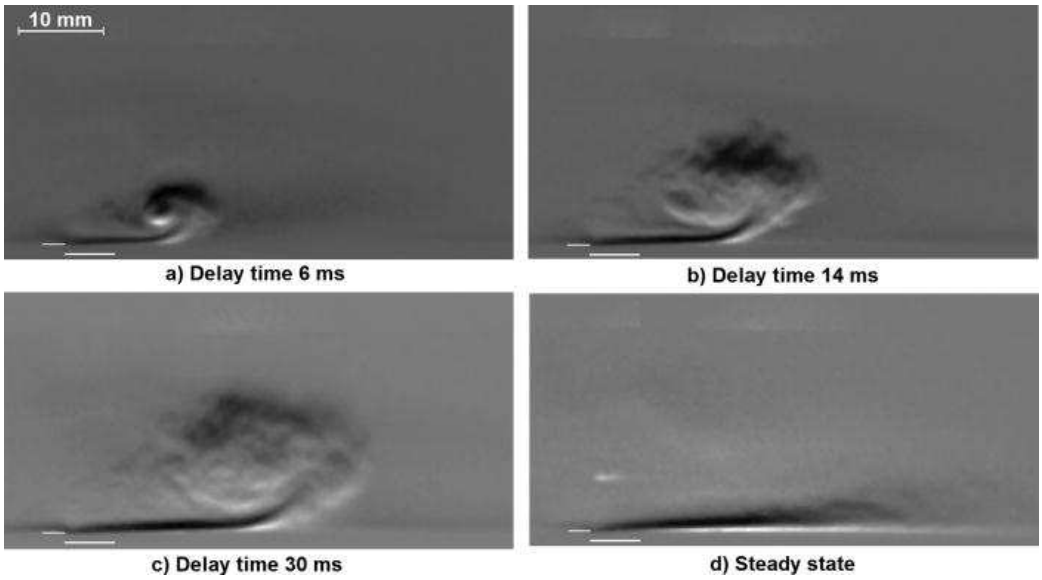

Figure 3.1: evolution of plasma jet. (Image from Cristofolini, Neretti)

The factors we changed throughout the experiment, our variables then, are the jet orientation angle , and the jets, which are distributed on the airfoil as shown in picture 2.14. The parameter that let us measure the effectiveness of plasma actuators is $\Delta C_{L\%}$ defined as:

$$\Delta C_{L\%} = \frac{C_L - C_{Lref}}{C_{Lref}} \qquad (3.2)$$

Where $C_{L\ ref}$ is the lift coefficient when plasma actuators are off, measured at one degree past the stall angle. C_L is, instead, the one measured at the same angle of attack but with actuators on.

3.1 Airfoil characterisation

Once the actuators were installed, the airfoil is not a perfect NACA 0015 anymore. In fact, the electrodes introduce concentrated roughness that, at low Reynolds numbers as in our case, can lead to the generation of a laminar separation bubble. This separation bubble influences the stall condition, in fact, the C_L-α graphs obtained after we put the actuators clearly differ from the clean airfoil ones. The results of the characterisation are shown in fig. 3.2.

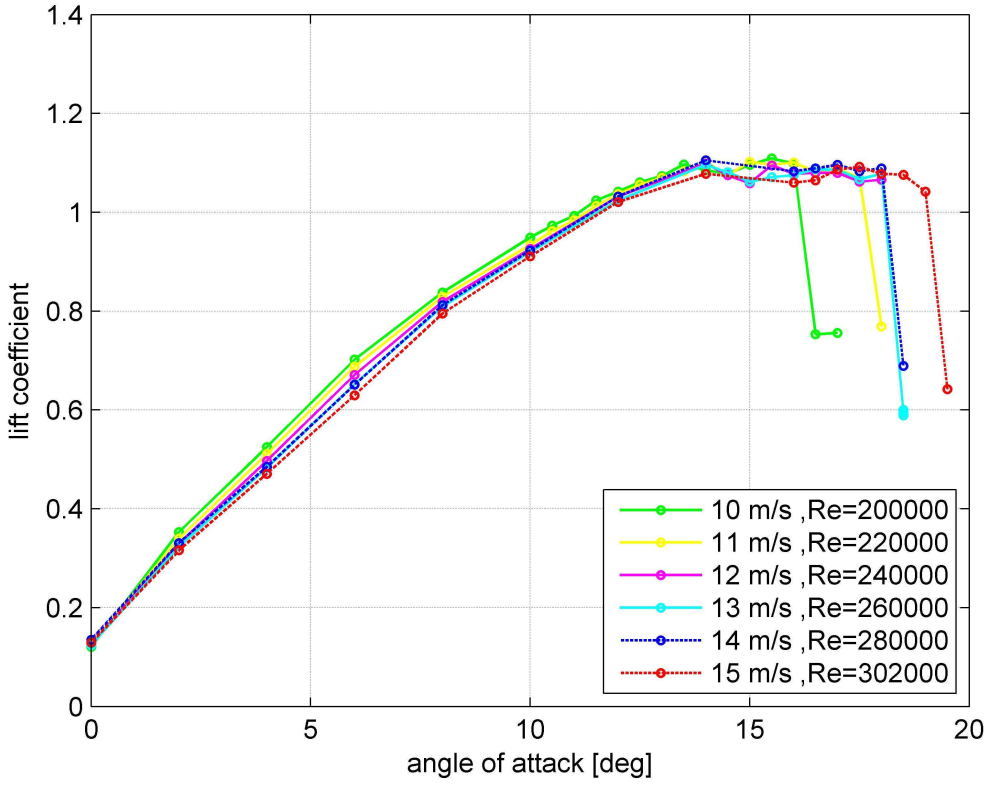

Figure 3. 2: NACA 0015 C_L- α graph with actuators installed on the upper and lower surfaces

To test actuators' effectiveness we focused on velocities up to 11 m/s. This choice is mainly due to the fact that after this value, the C_L-α curves haven't a sharp peak, and so it is hard to identify a reference point to see how the actuation of plasma actuators influence the boundary layer separation.

In fig. 3.3 and 3.4 it is possible to have an idea about the evolution of the maximum lift coefficient $C_{L,\,max}$ and of the stall angle α_{max} with Reynolds number.

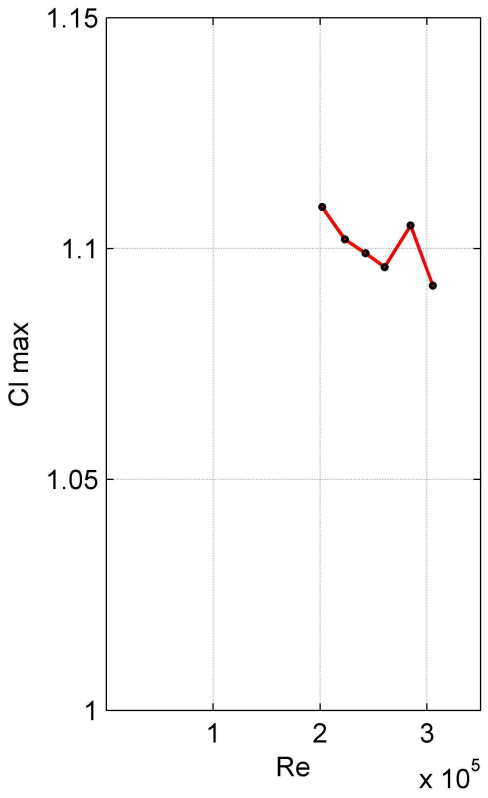

Figure 3. 3:maximum lift coefficient with Reynolds number

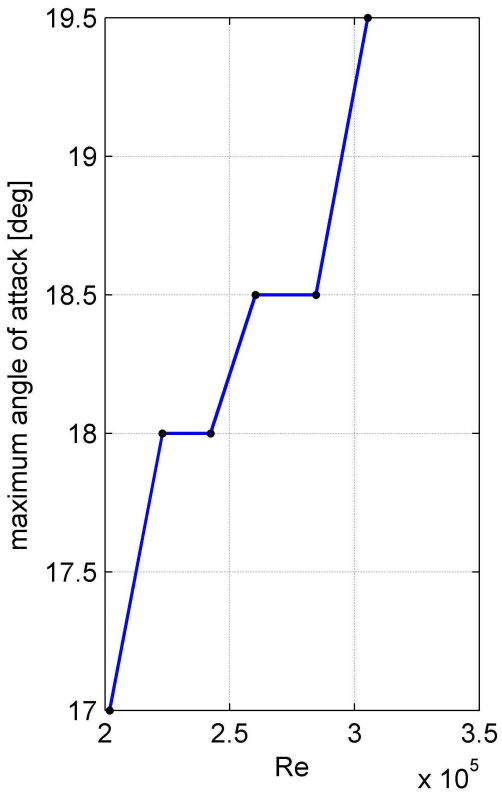

Figure 3.4: stall angle trend with Reynolds number

3.2 Steady actuation data analysis

As previously said, we turned the actuators both in steady and unsteady actuation. In particular, we started our experimental chain activating all actuators one by one or two together in steady actuation. We performed this test at 11 m/s because it is the highest velocity at which the plasma actuator's effect is well rendered. The aim of this first test was to identify which actuators, and consequently which jets, perform the best.

From the analysis of the data obtained, it is possible to conclude that the jets which have a major effect in terms of gain in lift coefficient are jet 5 and jet 6, as seen in fig. 3.5. Jet 5 is the one produced by the activation of actuator 5, the one exactly on the leading edge, and actuator 4, the one on the upper surface near the leading edge. Jet 6, instead,

is generated by the activation of actuator 5 and 6, the one near the leading edge but located over the lower surface.

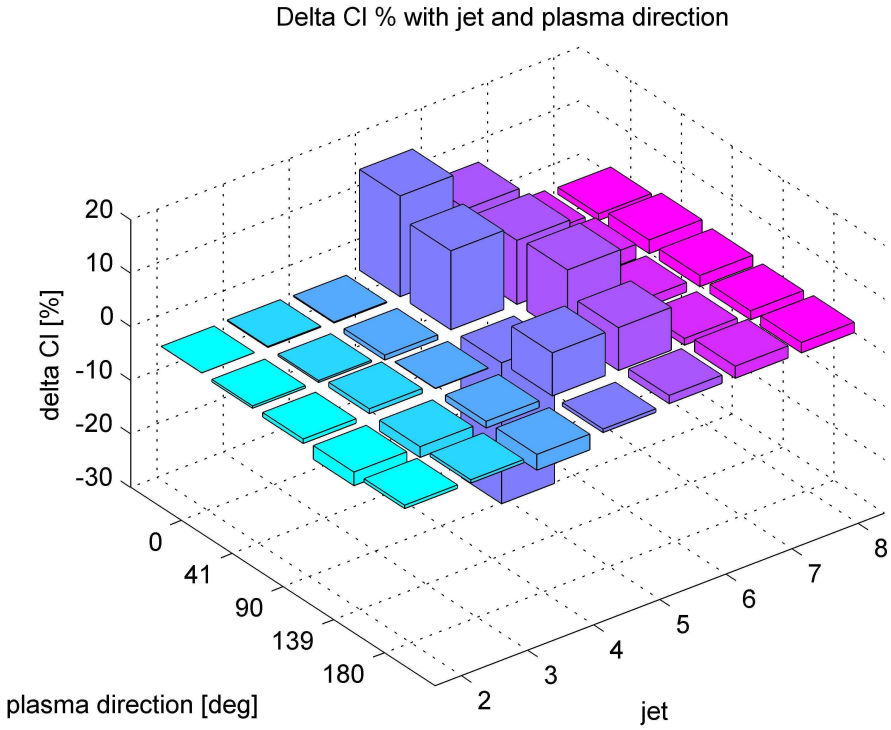

Figure 3. 5: $\Delta C_{L\%}$ with plasma direction and jet at 11m/s

At a first glance it is possible to notice how the gain in lift coefficient is never over 18.8% . This maximum value is achieved with jet 5 at ϑ=0°, therefore, powering only actuator 5. Despite being the best result for this configuration, it doesn't allow a complete recovery from stall condition.

Good results, although slightly under the percentages obtained with jet 5, are achieved also with jet 6. In this case in particular, vectoring reveals to be useful: orientating jet 6 at ϑ=41° and ϑ=90° let us reach a $\Delta C_{L\%}$ Of 11.9% and 12.6% respectively.

3.3 Jet 5 steady configuration

Since jet 5 proved to be the configuration with highest performances in steady actuation, we decided to concentrate on this jet and explore its effectiveness at lower velocities. In particular, we chose 5m/s, 7 m/s, 9 m/s and 11 m/s.

To avoid the doubts of which reference point to choose, the airfoil configuration was the same for each velocity. In particular, once found the stall angle for 11 m/s, we oriented the airfoil one angle past this value. As deducible from fig. 3.1 the angle of attack of our test configuration is 19.5° .

In the graphs below, in fig. 3.6, are presented the results for each velocity.

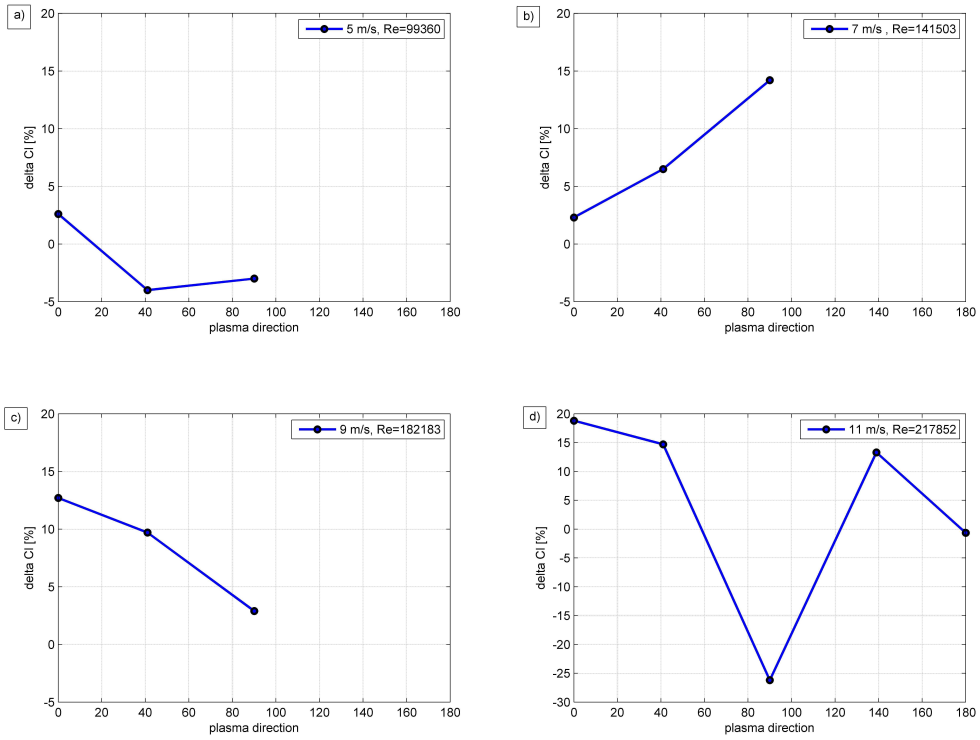

Figure 3. 6: $\Delta C_{L\%}$ with plasma direction at a) 5m/s b) 7m/s c) 9m/s d) 11m/s

From a first analysis and comparison between the graphs it is clear that the best result is achieved at 11 m/s, ϑ=0°, with a gain in C_L of 18.8%.

Overall, even at 7 m/s and 9 m/s is possible to obtain remarkable results, or at least comparable to the previous configuration. In fact, the $\Delta C_{L\%}$ is only slightly lower, reaching a maximum value of about 15% and 13% respectively. In particular, at 7 m/s this result is measurable at ϑ=90° (activating both actuator 4 and 5 then), while at 9 m/s for a jet orientation angle of 0°. It is important to stress how for these configurations we can always talk about gain, since the percentages are never negative. An exception is made for 5 m/s and 11 m/s. At 5 m/s for ϑ=41° a negative value have been measured. However, it is only slightly less than zero, therefore, negligible since we have to con-

sider possible errors linked to measurements. A significant negative value is present at 11m/s, for ϑ=90°, reaching almost –26%, but it is the only remarkable loss witnessed.

3.4 Jet 5 unsteady configuration

Once finished the tests in steady actuation, we moved to the unsteady one. In particular, the duty cycle was of 50% and the range of frequencies tested varied from a minimum of 5Hz to a maximum of 70Hz. In this case then, another variable has to be added, the frequency.

The method used to carry on the tests in unsteady actuation is the same as for the steady, and even the airfoil configuration is.

For each velocity it is possible to see the influence of frequency on the $\Delta C_{L\%}$.

The best results are seen at 7 m/s (fig. 3.7).

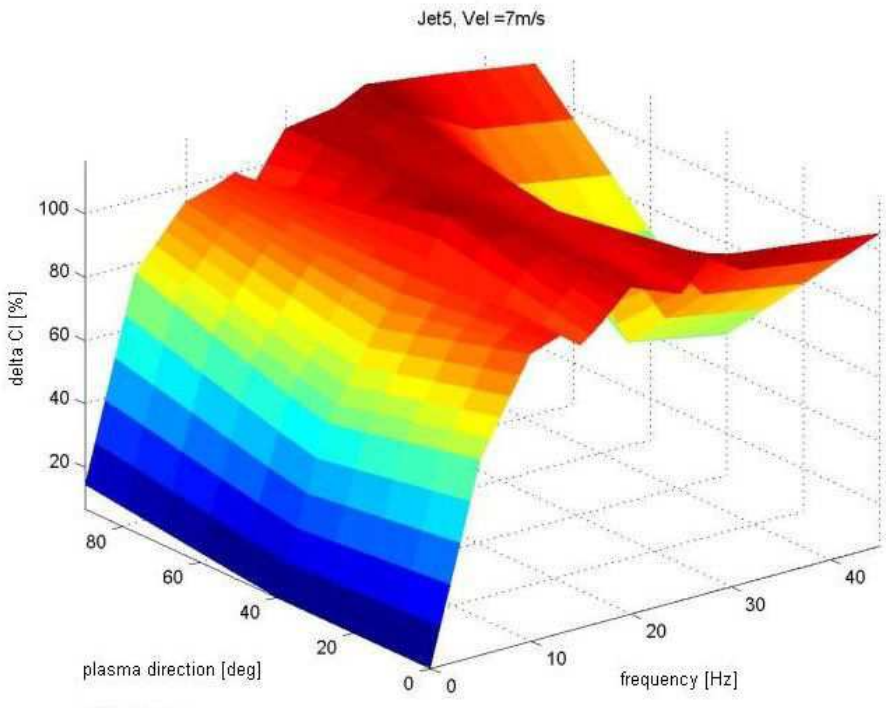

Figure 3.7: 3D graph of jet 5. $\Delta C_{L\%}$ with plasma direction and frequency is shown at 7m/s.

In this configuration, in fact, the percentages, from 5Hz to 40Hz are all over 70%, which means a complete recovery from stall condition, letting the boundary layer to re-

attach. The peak, of 117%, is seen at ϑ=90°, for a frequency of 28Hz. The trend of $\Delta C_{L\%}$. with frequency 3.8 below.

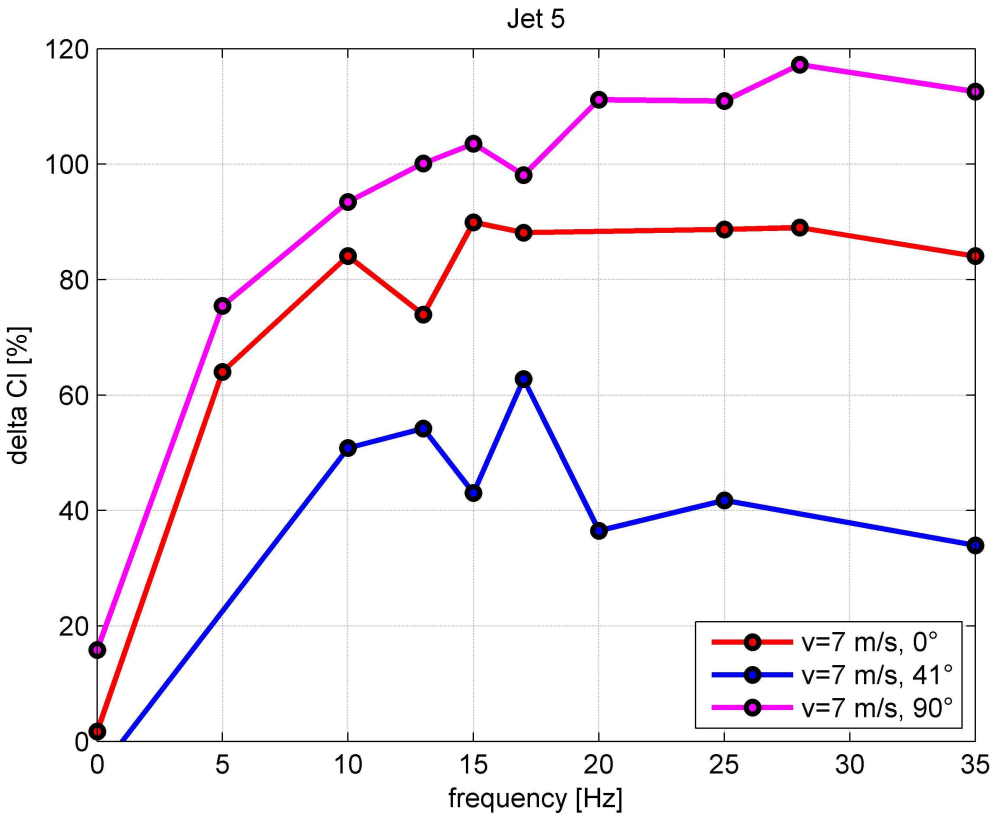

Figure 3.8: Jet 5 oriented at 0°,41°, 90°. $\Delta C_{L\%}$ with frequency is shown.

Remarkable results are obtained also at 9 m/s. In this case, the maximum $\Delta C_{L\%}$ is about 113% at ϑ=90°, f=28Hz. In general, as shown in fig. 3.9, the gain is never less than 63%, which occurs at ϑ=90°, f=5Hz and the behaviour between 10 and 55 Hz is more constant than in other velocities regimes, varying from 100 to 110%.

As for 11 m/s, it is clear from fig. 3.11 that the jet orientation angle that let us achieve the best result of 48.8% is 90°. In particular the highest percentage is reached at f=35Hz, as can be seen in fig. 3.12.
Overall the trend at 11 m/s presents a wide range of frequencies, namely from 10Hz to 45Hz, that allows the complete recovery from the stall condition, since the gain in C_L is always over 35%. In order to witness a decay in performances, it is necessary to reach very high frequency, 60-75 Hz.

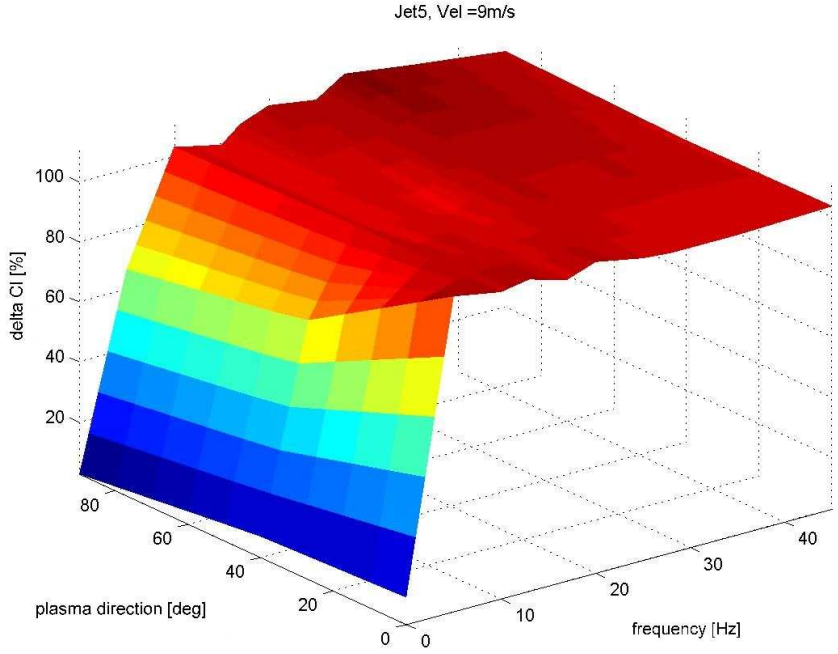

Figure 3.9: 3D graph of jet 5. $\Delta C_{L\%}$ with plasma direction and frequency is shown at 9m/s.

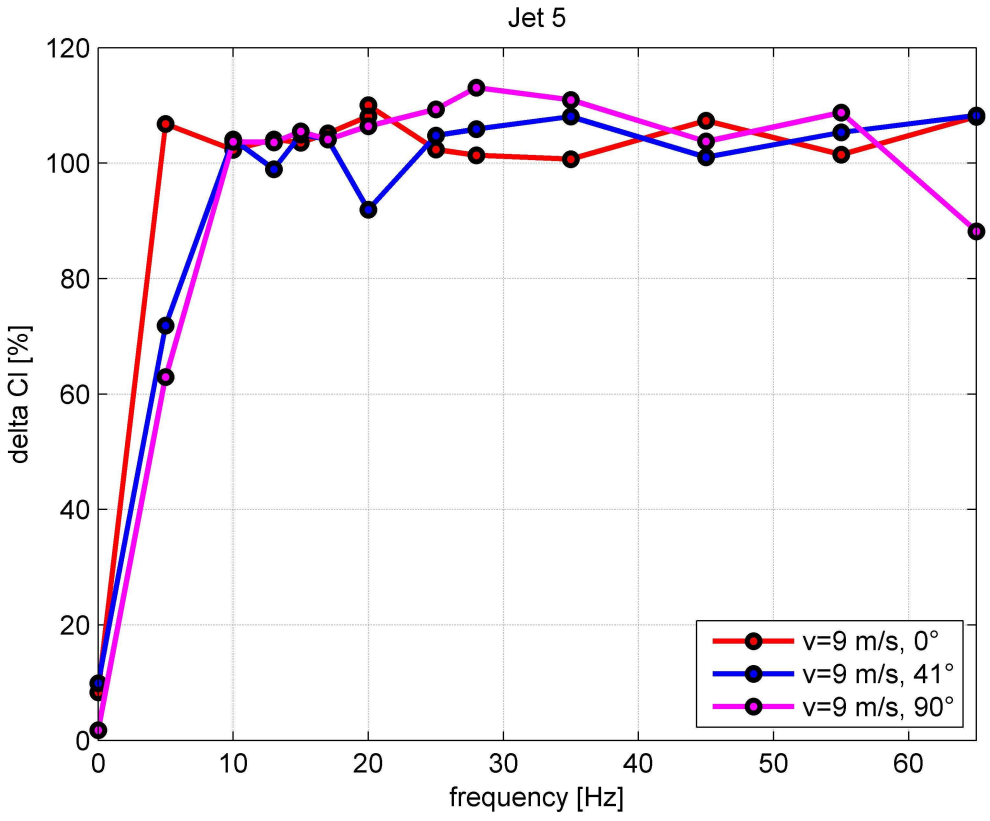

Figure 3. 10: Jet 5 oriented at 0°,41°, 90°. $\Delta C_{L\%}$ with frequency is shown

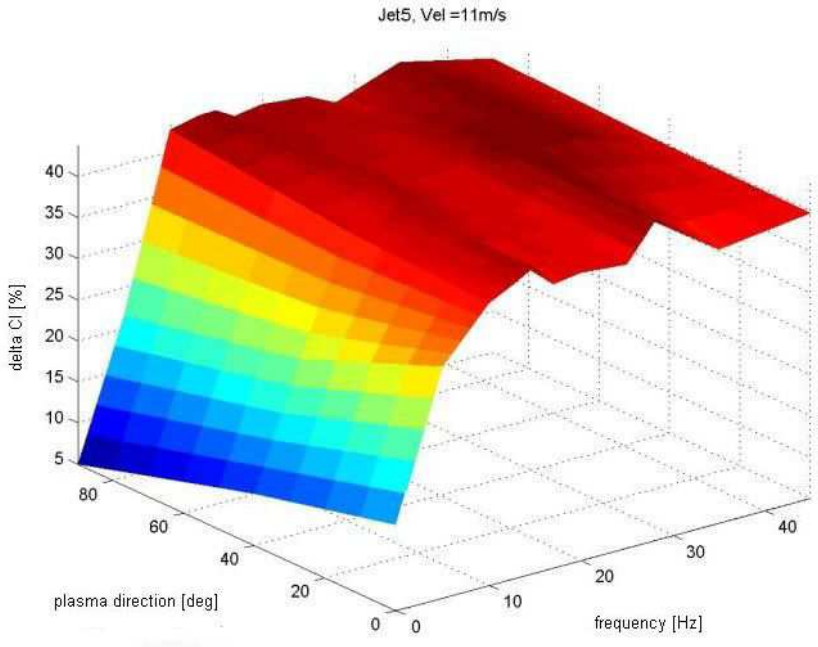

Figure 3. 11: 3D graph of jet 5. $\Delta C_{L\%}$ with plasma direction and frequency is shown at 11m/s. For jet 5 oriented at 0° measures for frequencies from 55Hz to 75Hz weren't performed since the decay was visible since 45Hz.

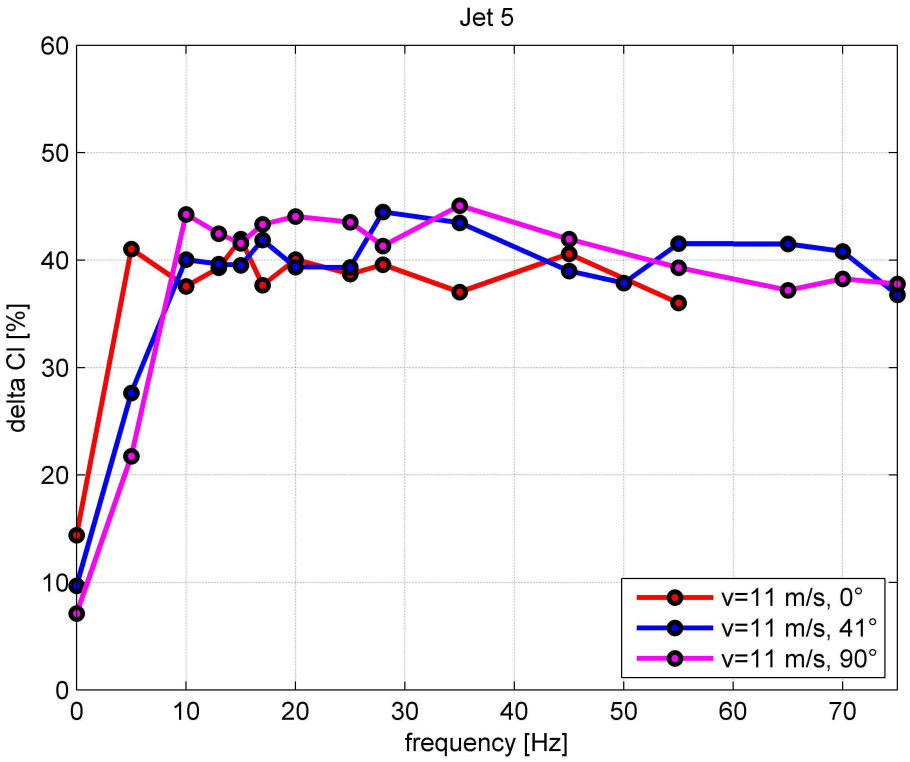

Figure 3. 12: Jet 5 oriented at 0°,41°, 90°. $\Delta C_{L\%}$ with frequency at 11 m/s is presented

The lowest velocity we tested the actuators' effectiveness at is of 5 m/s. The performances are slightly better than the ones observed at 11 m/s, reaching a maximum of 77% for ϑ=0° and f=10Hz, as shown in figure 3.13. In general, the best results are obtained for frequencies between 5 and 10 Hz.

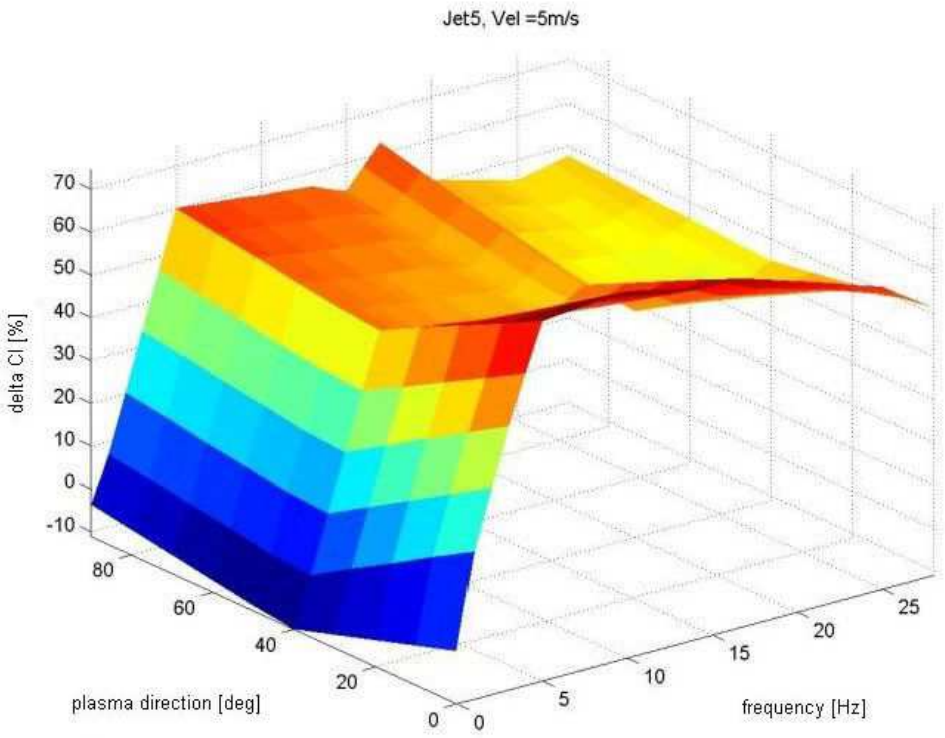

Figure 3. 13: 3D graph of jet 5. $\Delta C_{L\%}$ with plasma direction and frequency is shown at 5m/s.

In particular the trend of the $\Delta C_{L\%}$ with the frequencies is presented in fig. 3.14.

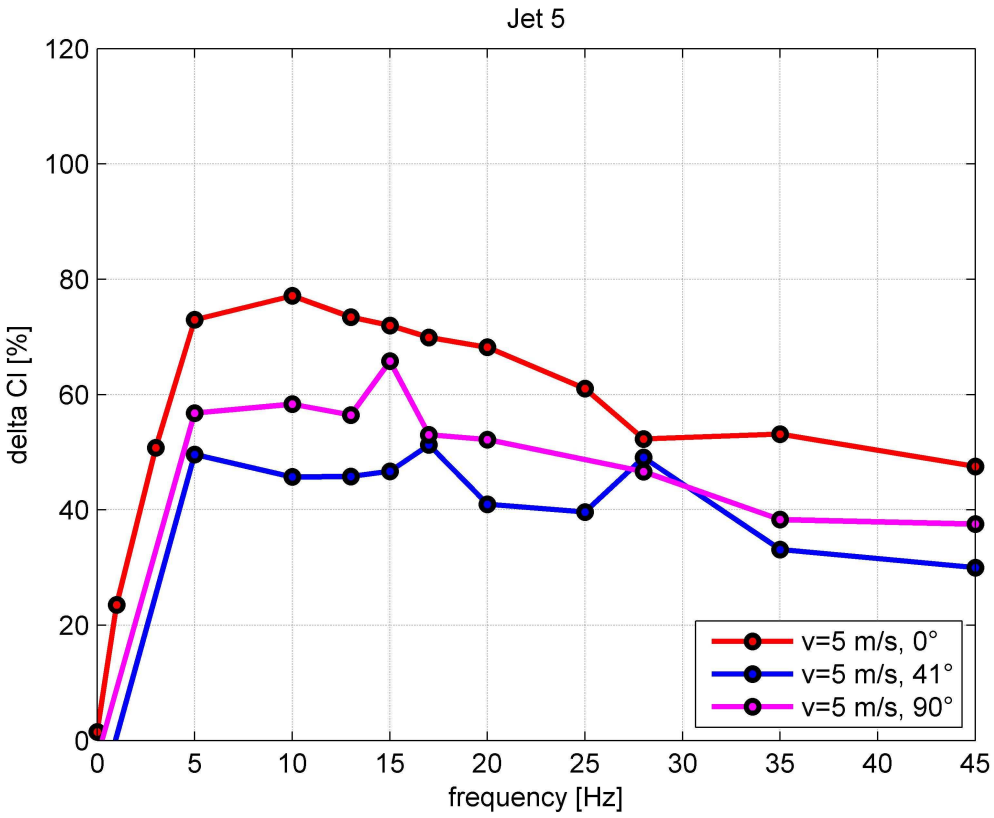

Figure 3. 14 Jet 5 oriented at 0°, 41°,90°. $\Delta C_{L\%}$ with frequency at 5 m/s is presented

Overall, all jet 5 configuration in unsteady actuation lead to a complete stall recovery, apart from the configuration at 11 m/s *f*=5 Hz, where the percentage is only scarcely above 20%.

In general, in picture 3.15 is possible to see how the frequency of maximum $\Delta C_{L\%}$ varies with velocity. The results are presented for the tested velocities of 5 m/s, 7m/s, 9m/s, 11 m/s.

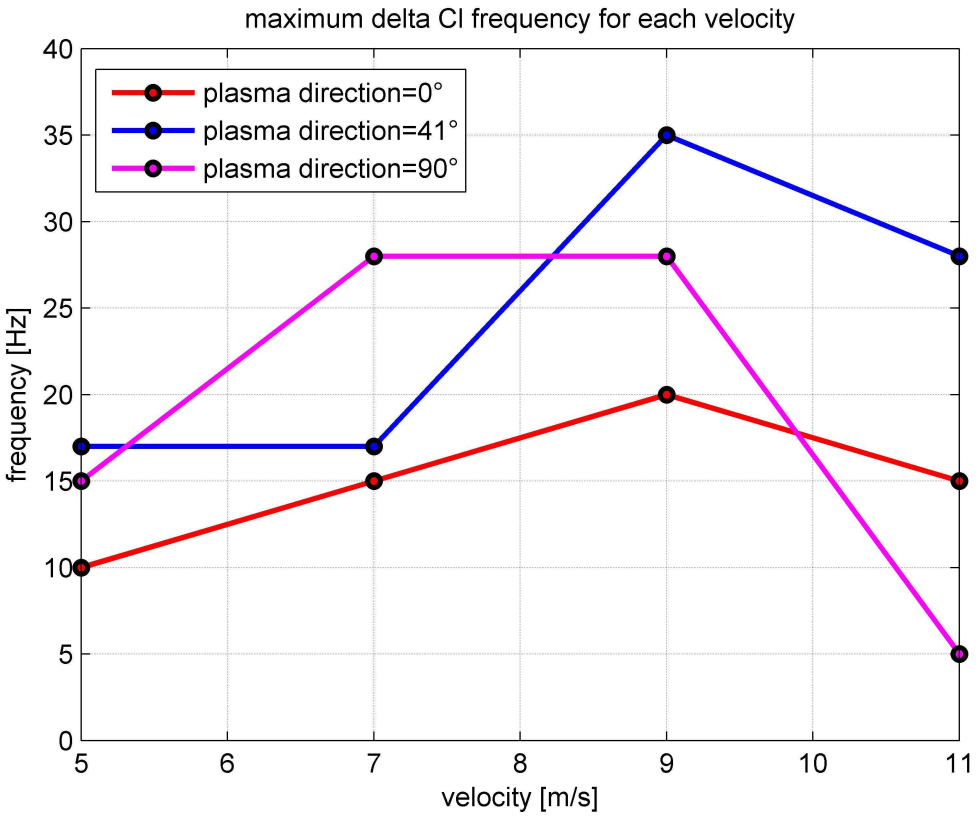

Figure 3.15: Maximum $\Delta C_{L\%}$ frequency for each velocity tested

3.5 Global comparison

From the analysis of the data presented, since jet 5 is the one that gives the best results, we can deduce that the actuators near to the leading edge are those who have the major effectiveness. In general, for steady actuation, the jet orientation angle ϑ, which let us achieve the highest percentage of 18.8, is 0°. Therefore only actuator five needs to be powered.

Overall, we can easily conclude that unsteady actuation leads to clearly better results than the steady one. Firstly, the gains obtainable from steady actuation are lower than 35%, so it does not let the airfoil recovery from stall. Secondly, in unsteady actuation, unlike the steady one, almost every configuration allows a gain in terms of C_L. Only exception is made for $\vartheta = 90°$ $f = 10$Hz, where a loss of –4% occurs. This negative per-

centage is slightly less than zero and inside the range of measurement error (up to 4%), so it can be considered negligible.

However, the best performance measured is obtained at 7 m/s, ϑ=90° (therefore activating both actuators 4 and 5) . The peak reached is of 117%, allowing a complete recovery from stall.

This is a positive aspect, since it is possible to reach maximum performances spending half of the power we should spend in steady operation. This is, without any doubts, an economical advantage.

This considerations proves that with plasma actuators on, and in particular vectoring the plasma, there's an effective boundary layer reattachment on leading edge, due to plasma action, which gives enough kinetic energy to tear down local adverse pressure gradients, that earlier has generated a separation bubble.

CONCLUSIONS

This thesis provides an experimental analysis of the effectiveness of oriented DBD plasma actuators over a NACA 0015 airfoil at low Reynolds numbers.

After the experimental analysis of different configurations, this thesis proves the effectiveness of oriented DBD plasma actuators in this situation, in particular at one angle past the stall angle.

The present results show that best performances of oriented plasma actuators are achieved activating the actuator located on the leading edge and, in general, the two installed on the upper and lower surfaces nearby leading edge. In other actuators the kinetic energy released is not enough to tear down the adverse pressure gradient on airfoil upper surface, and therefore to allow boundary layer reattachment. Moreover, sometimes it is possible to notice how orienting plasma jet at a specific angle could lead to loss in terms of lift coefficient value. Plasma vectoring let us achieve excellent results, but in steady operation, the jet orientation has to be chosen carefully.

However, superior performances are characteristic of unsteady actuation. This has proved to be best than the steady one in every case analysed, allowing almost always a gain in terms of C_L. The only exception measured is, anyway, slightly lower than zero, so negligible. Unsteady actuation, leads to more important results than the steady one, letting the airfoil completely recovery from stall condition. This results are positive, since unsteady operation reduces energy consumption, therefore gives us the possibility to decrease power supply system weight and dimensions, favouring a step forward to onboard aircraft applications.

In general we can conclude that, since the maximum and other excellent results are obtained with a 90° jet orientation, oriented DBD plasma actuators bring an improvement in plasma actuators technology.

BIBLIOGRAPHY

"Elements of fluid dynamics", Guido Buresti, Imperial College Press, 2012

"Low speed wind tunnel testing", J.B. Barlow, W.H. Rae Jr., A. Pope, Wiley-Interscience, 1999

"Adaptive flow control of low-Reynolds number aerodynamics using dielectric barrier discharger actuator", Young-Chang Cho, Wei Shyy, Journal, 2011

"Airflow control by non-thermal plasma actuators", E. Moreau, Journal, 2007

"Dielectric Barrier Discharge plasma actuators for flow control", T.C. Corke, C.L. Enloe, S.P. Wilkinson, Journal, 2009

"Flow control over a NACA 0012 airfoil using dielectric barrier discharge plasma actuators with a Gurney flap", Li-Hao Feng, T.N. Jukes, Kwing-So Choi, Jin-Jun Wang, Journal, 2012

"Laminar flow control research at TsAGI: past and present", S.L. Chernyshev, A.Ph. Kiselev, A.P. Kuryachii, Journal, 2010

"Plasma actuators for airflow control: measurements of the non-stationary induced flow velocity", M. Forte, L. Leger, J. Pons, E. Moreau, G. Touchard, Journal, 2005

"SDBD plasma enhanced aerodynamics: concepts, optimization and applications", T.C. Corke, M.L. Post, D.M. Orlov, Journal, 2007

“Single dielectric barrier discharge plasma enhanced aerodynamics: physics, modeling and applications”, T.C. Corke, M.L. Post, D.M. Orlov, Journal, 2007

“Simulations of flow separation control using plasma actuators”, Y.B. Suzen, P.G. Huang, Journal, 2006

Luca Ginepri’s MSc thesis, Università di Bologna, A.A. 2011/2012

Matteo Montecchia’s thesis, Università di Bologna, A.A. 2011/2012

ACKNOWLEDGEMENTS

RINGRAZIAMENTI

È mio vivo desiderio ringraziare tutti coloro che, con la loro collaborazione, mi hanno accompagnato in questo percorso e hanno reso possibile il raggiungimento di questo risultato.

Desidero innanzitutto ringraziare il Professor Alessandro Talamelli, per avermi dato la preziosa opportunità di approcciarmi al mondo lavorativo in ambito aerodinamico, per avermi fornito, con i suoi insegnamenti e la sua esperienza, gli strumenti necessari per approfondire molteplici aspetti teorici di questa materia.

Ringrazio anche l'Ing. Alessandro Rossetti, che con pazienza, ha messo a disposizione la sua esperienza guidandomi per tutta la durata dell'attività formativa.

Infine, ringrazio la mia famiglia, il cui supporto mi ha permesso di raggiungere questo importante traguardo.